

Superconducting circuit optomechanics in topological lattices

Amir Youssefi,^{1,*} Andrea Bancora,^{1,*} Shingo Kono,^{1,*} Mahdi Chegnizadeh,¹ Tatiana Vovk,¹ Jiahe Pan,¹ and Tobias J. Kippenberg^{1,†}

¹ Institute of Physics, Swiss Federal Institute of Technology Lausanne (EPFL), Lausanne, Switzerland

Cavity optomechanics enables controlling mechanical motion via radiation pressure interaction [1–3], and has contributed to the quantum control of engineered mechanical systems ranging from kg scale LIGO mirrors to nano-mechanical systems, enabling entanglement [4, 5], squeezing of mechanical objects [6], to position measurements at the standard quantum limit [7], non-reciprocal [8] and quantum transduction [9]. Yet, nearly all prior schemes have employed single- or few-mode optomechanical systems. In contrast, novel dynamics and applications are expected when utilizing optomechanical arrays and lattices [10], which enable to synthesize non-trivial band structures, and have been actively studied in the field of circuit QED [11–14]. Superconducting microwave optomechanical circuits are a promising platform to implement such lattices [15], but have been compounded by strict scaling limitations. Here we overcome this challenge and realize superconducting circuit optomechanical lattices. We demonstrate non-trivial topological microwave modes in 1-D optomechanical chains as well as 2-D honeycomb lattices, realizing the canonical Su-Schrieffer-Heeger (SSH) model [16–18]. Exploiting the embedded optomechanical interaction, we show that it is possible to directly measure the mode functions of the bulk band modes, as well as the topologically protected edge states, without using any local probe [19–21] or inducing perturbation [22, 23]. This enables us to reconstruct the full underlying lattice Hamiltonian beyond tight-binding approximations, and directly measure the existing residual disorder. The latter is found to be sufficiently small to observe fully hybridized topological edge modes. Such optomechanical lattices, accompanied by the measurement techniques introduced, offers an avenue to explore out of equilibrium physics in optomechanical lattices such as quantum [24] and quench [25] dynamics, topological properties [10, 26, 27] and more broadly, emergent nonlinear dynamics in complex optomechanical systems with a large number of degrees of freedoms [28–31].

Mechanical oscillators can exhibit modes with ultralow mechanical dissipation and compact form factors due to the slow velocity of acoustic waves, and are already used in applications ranging from timing [32] to wireless filters [33]. Over the past decade, novel ways in which mechanical systems can be quantum controlled have been

developed, based on either coupling to electromagnetic cavities in quantum optomechanics [1–3] or superconducting qubits in quantum acoustics [34]. The former route has utilized the coupling to electromagnetic cavities both in the optical and microwave domain, and enabled to reach a regime where the quantum nature of the optomechanical interaction becomes relevant [35, 36]. This has allowed a host of manipulations of mechanical systems, including cooling mechanical systems to the ground state [37, 38], state transfer [39], remote entanglement of mechanical oscillators [40], or generation of squeezed mechanical states [6]. In addition, such systems have been employed for quantum microwave to optical transduction [9].

The majority of optomechanical systems, which have probed classical as well as quantum properties and dynamics, have utilized 'few-mode' optomechanics, i.e. systems that employ a small number of optomechanical degrees of freedom. Pioneering theoretical works have predicted that significantly richer and novel dynamics can be accessed in optomechanical lattices including topological phases of light and sound [10], collective [41–43] and quench [25] dynamics, quantum many-body dynamics [24] and entanglement [28], non-reciprocity [29], reservoir engineering [30], and soliton generation [31]. To date, such optomechanical lattices have only been realized via mechanically mediated coupling [44] – similar to studies that employ mechanical meta-materials [45]. Indeed, while the coupling of mechanical oscillator for acoustic metamaterials has been successfully achieved [46, 47], implementing optomechanical lattices has been a long-lasting challenge. Topological phonon transport has recently been reported in optomechanical crystals [48], consisting of coupled mechanical oscillators, however, site-by-site engineerable optomechanical lattices of coupled microwave or optical cavities, have not yet been realized due to the stringent requirements on identical individual optomechanical sites. To realize optomechanical lattices that include photon transpor, it is imperative that the disorder in the optical (or microwave) cavity is sufficiently small to enable building lattice models.

Superconducting circuit optomechanical systems based on vacuum-gap capacitors [37, 49] are a very promising platform to realize such lattices, and have been employed in a wide range of experiments, including ground-state cooling [15], mechanical squeezing [6], entanglement [4, 5, 50] of mechanical motion, dissipative quantum reservoir engineering [51], realization of hybrid qubit-mechanical systems [39, 52, 53], as well as non-reciprocal microwave devices [8]. While microwave planar res-

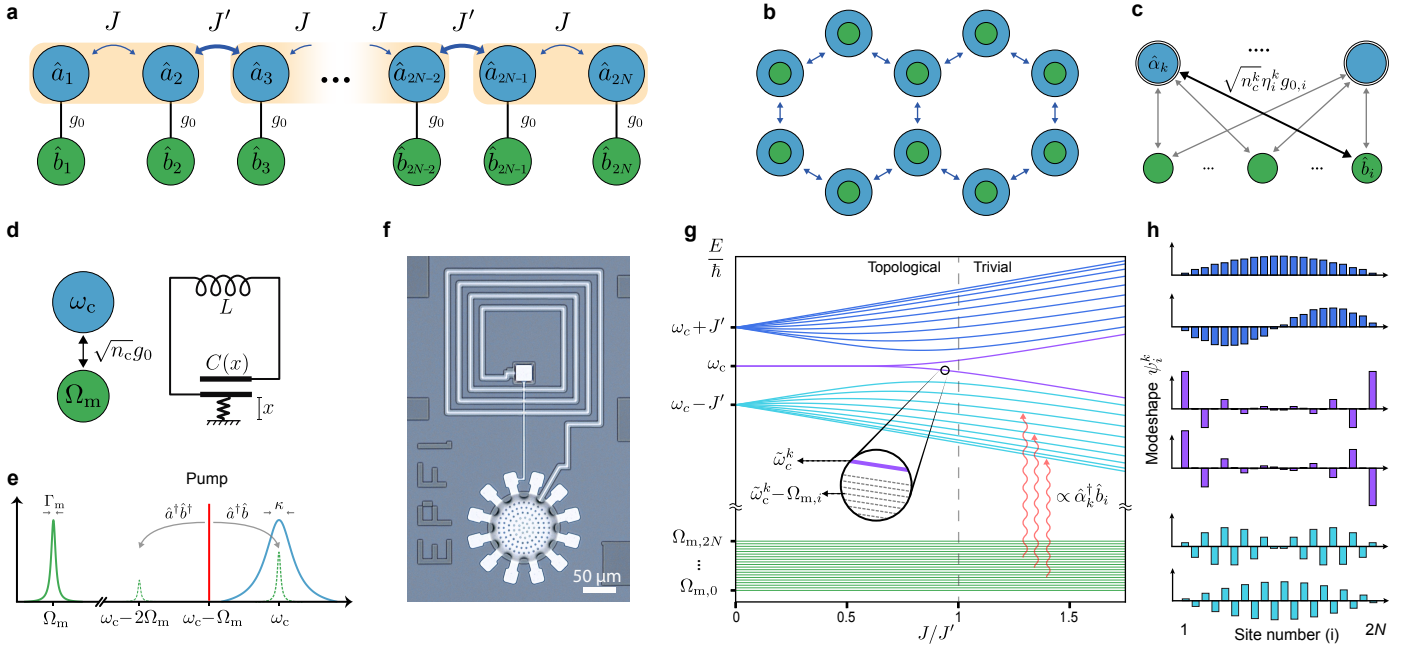


FIG. 1. Optomechanical lattices composed of microwave superconducting optomechanical systems as unit cells

a, Mode diagram of an optomechanical array with staggered mutual couplings demonstrating the Su-Schrieffer-Heeger model in the topological phase. Electromagnetic and mechanical modes are shown by blue and green circles correspondingly. **b**, An example of a two-dimensional optomechanical lattice. **c**, Equivalent mode diagram of the multimode optomechanical systems shown in **c** and **b**. Collective electromagnetic eigenmodes are coupled to all mechanical resonators by the effective optomechanical coupling rates which are proportional to their participation ratio, η_i^k . **d**, The equivalent circuit representation of an optomechanical site. **e**, Driving the electromagnetic cavity generates optomechanical sidebands. **f**, Micrograph of an optomechanical circuit with a mechanically compliant capacitor. **g**, Energy diagram of the array shown in **a** versus mutual coupling rates ratio. Photon-phonon transitions can be excited by sideband driving a collective electromagnetic mode. **h**, Collective electromagnetic mode shape examples of the two highest and lowest frequency modes as well as topological edge states calculated for $J_1/J_2 = 0.5$.

onators have been coupled and been used to create topological waveguides [11, 54], or higher order topological insulators [14] it has to date not been possible to realize optomechanical lattices in a similar fashion due to the technical challenge of reliably fabricating multiple vacuum-gap capacitors, with indentical mechanical and microwave properties.

Here we overcome this challenge, and demonstrate circuit optomechanical lattices in both 1-D (chains) and 2-D (honeycomb lattices), and use it to implement a topological band structure, exhibiting topologically protected edge states. Using the on-site optomechanical interactions, we are able to perform a direct measurement of the collective microwave mode shapes, reconstruct the full Hamiltonian of such multimode system beyond the tight-binding approximation, and demonstrate exceptionally low disorder in our devices. Such optomechanical mode shape measurements equally addresses an experimental challenge in large-scale multimode superconducting circuits as a platform for quantum simulation [55–57] and many-body physics studies [12, 13, 58], where only indirect approaches were performed by near field scanning probes [19], laser scanning microscopy [22, 23], or dispersive coupling to qubits [54].

Multimode optomechanics in lattices

With this motivation, we consider 1D and 2D lattices of optomechanical systems (see examples shown in Figs. 1a and b), where the building block (site) consists of a single mechanical and electromagnetic resonator coupled via radiation-pressure force as shown in Fig. 1d. the Hamiltonian of such lattice is described by

$$\hat{H}/\hbar = \sum_i \left(\omega_{c,i} \hat{a}_i^\dagger \hat{a}_i + \Omega_{m,i} \hat{b}_i^\dagger \hat{b}_i + g_{0,i} \hat{a}_i^\dagger \hat{a}_i (\hat{b}_i^\dagger + \hat{b}_i) \right) + \sum_{i \neq j} \left(J_{ij} \hat{a}_i^\dagger \hat{a}_j + J_{ji} \hat{a}_j^\dagger \hat{a}_i \right), \quad (1)$$

where \hat{a}_i and \hat{b}_i are the annihilation operators for the electromagnetic and mechanical modes with a resonance frequency of $\omega_{c,i}$ and $\Omega_{m,i}$ respectively at site i , $g_{0,i}$ is the single-photon optomechanical coupling rate, and J_{ij} is the coupling rate between electromagnetic modes i and j . As shown in Figs. 1d and e, the photon-phonon transitions can be excited by electromagnetically driving an optomechanical system, leading to an enhanced coupling rate of $g = \sqrt{n_c} g_0$, where n_c is the mean intracavity photon number. Figure 1f shows the physical realization of

the optomechanical site in the microwave superconducting circuit platform, consisting of an LC circuit with a mechanically compliant vacuum-gap capacitor.

In the weak optomechanical coupling regime, when the electromagnetic interactions dominate the system's dynamics, collective microwave modes are well defined as $\hat{\alpha}_k = \sum_i \psi_i^k \hat{a}_i$, where ψ_i^k is the normalized mode function of mode k . Using the collective mode basis, the total Hamiltonian is described as

$$\hat{H}/\hbar = \sum_k \tilde{\omega}_c^k \hat{\alpha}_k^\dagger \hat{\alpha}_k + \sum_i \Omega_{m,i} \hat{b}_i^\dagger \hat{b}_i + \sum_{k,i} (g_{0,i} \cdot \eta_i^k) \cdot \hat{\alpha}_k^\dagger \hat{\alpha}_k (\hat{b}_i^\dagger + \hat{b}_i), \quad (2)$$

where $\tilde{\omega}_c^k$ is the eigenfrequency of collective mode k and $\eta_i^k = |\psi_i^k|^2$ is the energy participation ratio of collective mode k at site i . As schematically shown in Fig. 1c, each collective microwave mode is parametrically coupled to all the mechanical oscillators with the weight of the corresponding participation ratio. Since each mechanical oscillator is locally coupled to a collective mode, their optomechanical interaction can be used as a local probe for the collective microwave mode in our measurements.

To show the characteristic mode shapes for a non-trivial topological phase, we apply the SSH model to optomechanical lattices. In the ideal 1D SSH chain, each unit cell consists of two optomechanical systems (sites) with an intra-cell electromagnetic coupling rate J , and an inter-cell coupling rate J' (see Fig. 1a). For an infinite chain, the energy spectrum can be analytically calculated and results in an upper and lower passband (UPB and LPB) separated by a band gap centered at ω_c (see SI). Similarly, in the case of a finite chain, when $J > J'$ (*trivial* phase), discrete modes will fit in such passbands. However, when $J < J'$ (*topological* phase) two so-called *edge* states separate from the passbands and appear in the middle of the band gap due to the truncated boundary condition of the chain, that are topologically protected [18]. Figure 1h shows the mode functions, ψ_i^k , for a few modes from the UPB, LPB, and the edge modes, which exhibit the chiral symmetry of the underlying lattice. In practice, disorder and imperfection disturb the mode shape, leading to the localization of the edge state. The existence of the edge states is evidence for the non-trivial topological properties [59].

Superconducting microwave optomechanical lattices

The main challenge of implementing circuit optomechanical lattices is the low reproducibility of the gap size of capacitors fabricated by the conventional process presented by Cicak *et al.* (2010) [49] where the movable plate had a non-flat geometry. This prevents accurate control of the gap size and consequently the mechanical and microwave frequencies, as well as their coupling strength.

To overcome this challenge, we developed a nanofabrication process that significantly improves reproducibility and controllability over the gap size. We realize a flat aluminum membrane as the movable capacitor plate suspended over a so-called trench (Figs. 2b, c, and d). In brief, we first etch a trench in a silicon substrate and cover it with an SiO_2 sacrificial layer. We then planarize the oxide layer to remove the topography and deposit the flat top plate of the capacitor. Finally, by removing the sacrificial layer, the top plate is suspended over the trench (Figs. 2b,e). Cooling down such a device induces a tensile stress in the Al thin film, which guarantees the flatness and consequently the gap size to be controlled by the trench depth (see SI for details). This high-yield process allows us to control microwave and mechanical resonance frequencies with fluctuations less than 0.5% and 1% respectively (see SI), a substantial improvement over previously employed approaches [60]. Moreover the approach benefits from low mechanical dissipation $\Gamma_m/2\pi \sim \mathcal{O}(1-10)\text{Hz}$ (c.f. SI) which as shown elsewhere [61] can reach exceptionally low values ($\Gamma_m/2\pi < 100 \text{ mHz}$).

To realize the topological optomechanical array (Fig. 1a), we fabricated a ten-site chain of mechanically compliant LC resonators with alternating mutual inductive coupling controlled by their physical distance (Figs. 2a, and f). The gap size is fabricated to be 245 nm, which results in a microwave frequency of $\omega_c/2\pi = 7.12 \text{ GHz}$ for all sites. The microwave coupling rates are designed to be $J/2\pi = 470 \text{ MHz}$ and $J'/2\pi = 700 \text{ MHz}$ to achieve the non-trivial topological phase.

Figure 2g shows the microwave transmission spectrum of the chain, the UPB and LPB are highlighted by the shaded areas, and two topological edge modes can be observed in the middle of the band gap. The transmission response is in good agreement with the calculated eigenfrequencies of the desired design (Fig. 2k) which indicates reliable control over the system parameters in the fabrication process. The linewidth of the modes varies from 7 MHz for the edge modes to 80 kHz for the first LPB mode depending on the collective mode shape. The asymmetry of the band structure in the transmission spectrum originates from the small parasitic mutual inductive coupling between distanced sites beyond the nearest neighbor (see SI) and does not change the topological properties of the chain [59, 62, 63].

The fundamental mechanical frequency of a drumhead capacitor (Fig. 2b inset) is inversely proportional to the trench radius, which is lithographically controlled. In order to identify each site by its mechanical frequency, we gradually increment the trench radius by 500 nm along the chain to distinguish them in further measurements.

Mechanical frequencies can be measured using optomechanically induced transparency (OMIT) [64, 65] by applying a microwave pump red-detuned from a collective microwave mode while sweeping a weak probe tone across the resonance, as shown in Fig. 2i. Figure 2h shows the OMIT response of the highest bulk mode. We observe ten

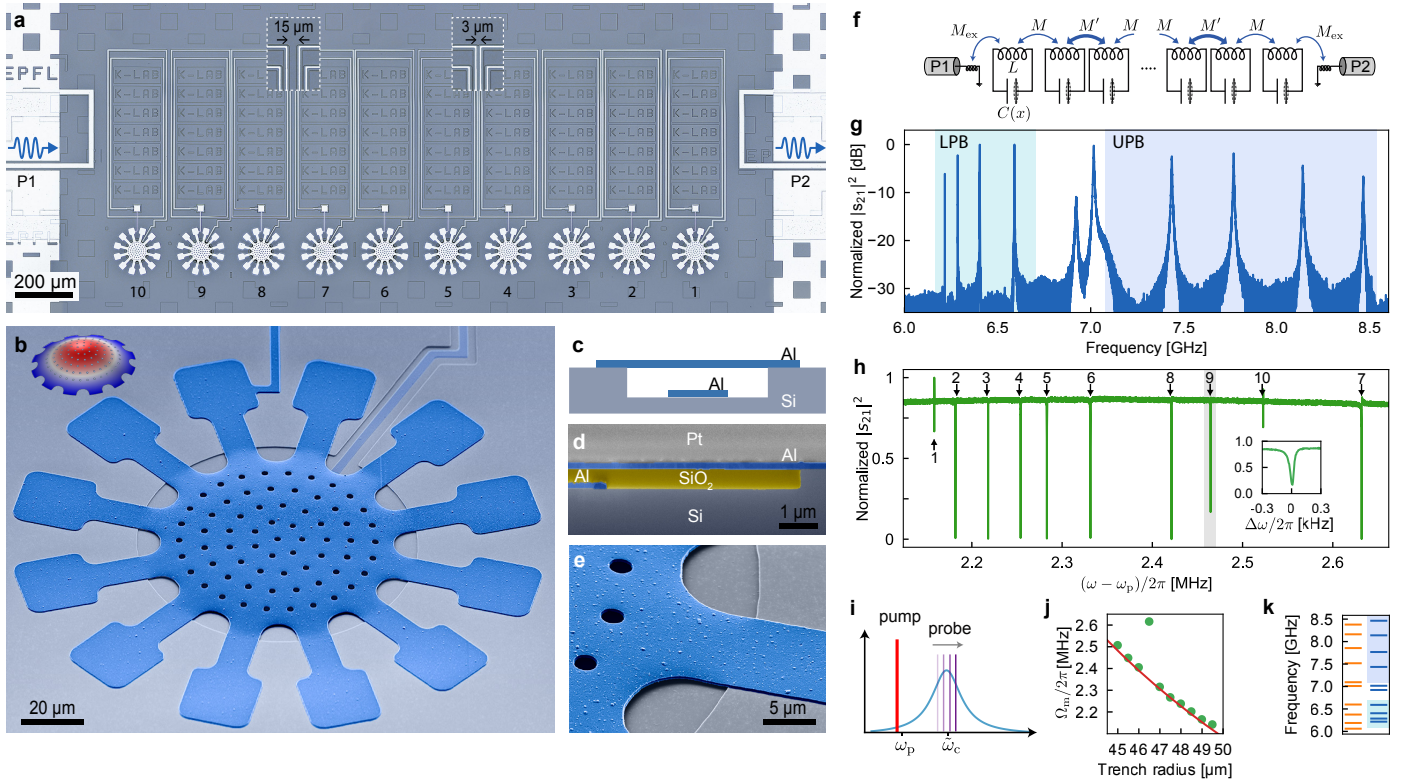


FIG. 2. Realization of circuit optomechanical 1-D chains. **a**, Optical micrograph of a 10 site SSH circuit optomechanical chain. The mutual coupling is controlled by the spacing between adjacent spiral inductors (see insets). The chain is inductively coupled at both edges to co-planar waveguides. **b**, SEM of a mechanically compliant vacuum-gap capacitor. The inset shows the FEM simulation of the fundamental mechanical mode of the vibrating plate. **c**, Schematic cross-section of the capacitor. **d**, Focused ion beam cross-section of a capacitor before removing the SiO_2 sacrificial layer (Pt is used as the FIB protective layer). **e**, SEM of a suspended clamp over the trench. **f**, Equivalent circuit diagram of the SSH chain. **g**, The transmission spectrum of the device shown in **a**; two topological edge modes are distinguished in the band gap. **h**, Optomechanical induced transparency (OMIT) response of the highest frequency collective microwave mode. OMIT features are linked to drumhead capacitors along the chain identified by the mechanical frequency. **i**, Frequency scheme for the OMIT measurement. **j**, Measured mechanical frequencies versus the trench radius (green dots). the solid line shows the inverse linear fit. **k**, Microwave resonance frequencies of the device, design targets (orange), and measured values (blue).

OMIT features indicating mechanical frequencies, matching the inverse trench radius relationship (Fig. 2j). One mechanical resonance is off due to an unusual deformation of the capacitor after the release.

Optomechanical mode shape measurement

Next we exploit mechanical resonators as embedded probes to directly and non-perturbatively measure the collective microwave mode shapes. We use the optomechanical damping effect [1] to link the mode shape information ($\sqrt{\eta_i^k}$) to the mechanical oscillator's dynamics. In the sideband resolved regime ($\kappa_{\text{tot}}^k \ll \Omega_{\text{m},i}$), the effective damping rate of a mechanical mode i , in the presence of a red-detuned pump from a collective microwave resonance k , is given by

$$\Gamma_{\text{eff},i}^k = \Gamma_{\text{m},i} + n_c^k \frac{4(\eta_i^k g_{0,i})^2}{\kappa_{\text{tot}}^k}, \quad (3)$$

where $\Gamma_{\text{m},i}$ is the bare mechanical damping rate, n_c^k and κ_{tot}^k are the photon number and the linewidth of the collective mode, respectively.

In a time-domain protocol, we apply an excitation pulse on resonance to generate a beat note with a pump red detuned by $\Omega_{\text{m},i}$ (Fig. 3b) and selectively excite a mechanical mode. Then we measure the ring down of the optomechanical sideband in the presence of the red-detuned pump. The slope of the Γ_{eff} variation with the pump power is proportional to η_i^k for a chosen collective microwave mode k , as shown in Eq. 3. Figure 3c shows the ringdown data sets for a few mechanical modes in the chain measured on the highest UPB mode. By measuring the effective damping rate of every site in the chain, the full mode shape can be extracted for the corresponding microwave mode. Although it is challenging to independently obtain several parameters in Eq. 3, such as $g_{0,i}$ and n_c^k , we can extract η_i^k from the slope of $\Gamma_{\text{eff},i}^k$ by using the normalization condition of $\sum_k \eta_i^k = \sum_i \eta_i^k = 1$

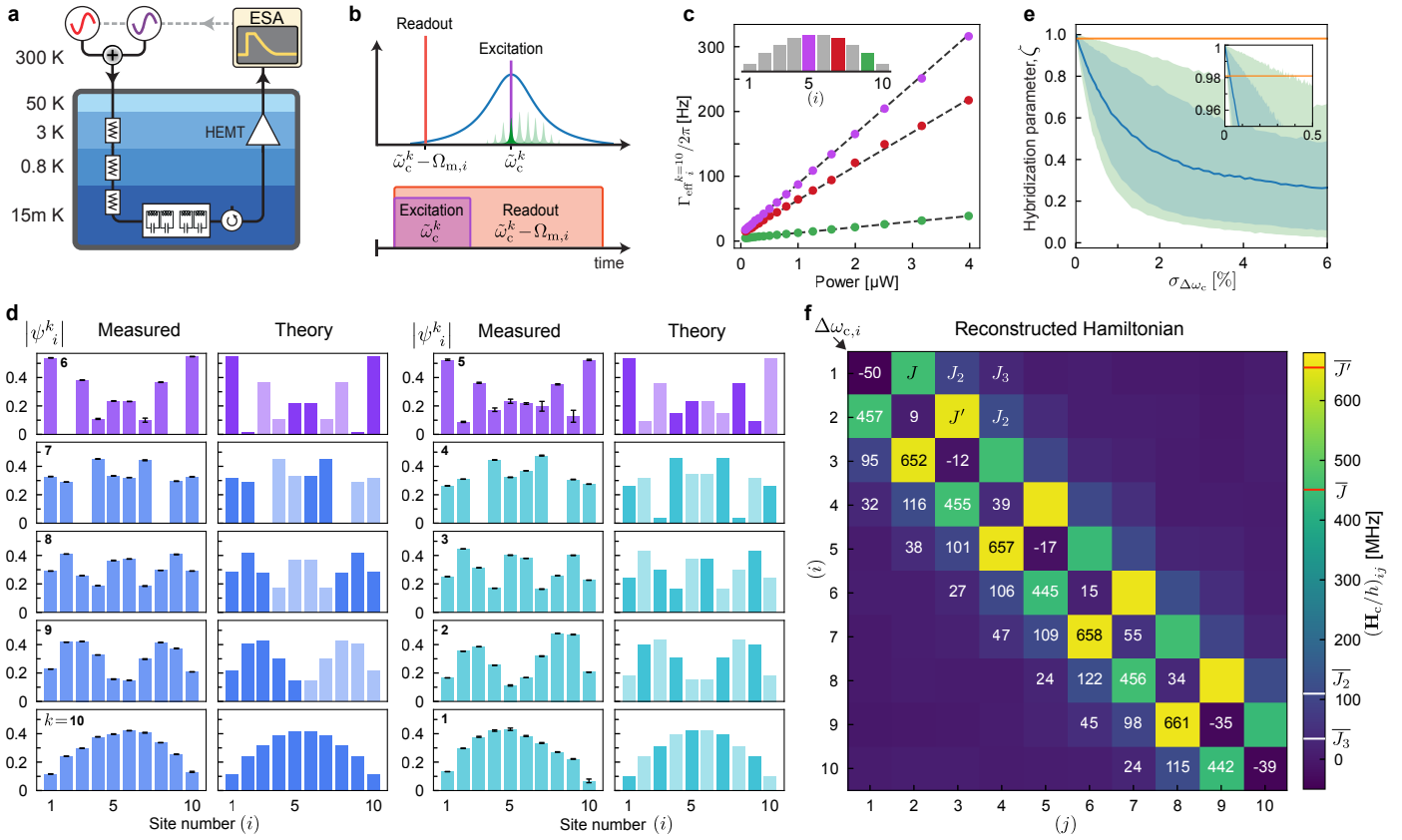


FIG. 3. Optomechanical collective mode shape measurement and Hamiltonian reconstruction of a topological SSH chain. **a**, Experimental setup for the mode shape measurement. **b**, Frequency and pulsing scheme: each mechanical mode is selectively driven by an on resonance excitation pulse while the red-detuned readout pump is on. **c**, Effective mechanical damping rate of the specific sites shown in the inset while driving the highest UPB mode. The slope of the linear fits depends on the collective mode shape. **d**, Measured and corresponding theory mode shapes of UPB, topological edge states, and LPB. Error bars are shown in black. In the theory plots, the phase information is encoded by different brightness. **e**, Stochastic analysis on the cavity frequency disorder effect on edge state hybridization quantified by ζ . The blue line shows expected value, blue and green shades reflect 70% and 90% certainties, and the orange line shows measured value. **f**, Reconstructed Hamiltonian matrix of the microwave subsystem in the rotating frame of the averaged cavity frequency. The diagonal elements show cavity frequency disorder, and off-diagonal ones show nearest neighbor couplings (J, J') as well as the parasitic couplings between distanced sites (J_2, J_3 , etc.).

(see SI for more details). Figure 3e shows the full result of the mode shape characterization on the ten site chain compared with the theoretical values with the design parameters. The data is in excellent agreement with the theoretical predictions, demonstrating bulk collective modes in UPB, LPB, and topological edge states.

In prior experimental realizations of the SSH model, non-hybridized topological edge states were observed [54, 66] (localized on only one side of the chain). The edge state hybridization strongly depends on the disorder in the system parameters. Here, in contrast, we observe fully hybridized topological edge states indicating minimal frequency fluctuation in the fabrication process. We perform a numerical stochastic analysis to study the effect of bare cavity frequency disorder on the edge modes hybridization, quantified by ζ . Figure 3e shows the expected value of ζ versus the standard deviation of the disorder $\sigma_{\Delta\omega}$ indicating less than 0.3% disorder in the

measured chain (see SI for more details).

Finally, considering the knowledge of all the eigenvectors (ψ_i^k , mode shapes) and eigenvalues ($\tilde{\omega}_c^k$, collective microwave frequencies) of the system, we can reconstruct the actual Hamiltonian of the microwave subsystem in the basis of physical sites:

$$\mathbf{H}_c/\hbar = \mathbf{U}_\psi^\dagger \begin{bmatrix} \tilde{\omega}_c^1 & & 0 \\ & \ddots & \\ 0 & & \tilde{\omega}_c^{2N} \end{bmatrix} \mathbf{U}_\psi \quad (4)$$

where $[\mathbf{U}_\psi]_{k,i} = \psi_i^k$ is a unitary matrix obtained from the measured participation ratios. Since our measurement protocol does not retrieve the phase of mode shapes, we inferred it from the theoretical mode shapes. To more accurately reconstruct the Hamiltonian, we correct the unitary matrix by further imposing the orthogonality condition (see SI for more details). Figure 3f shows the re-

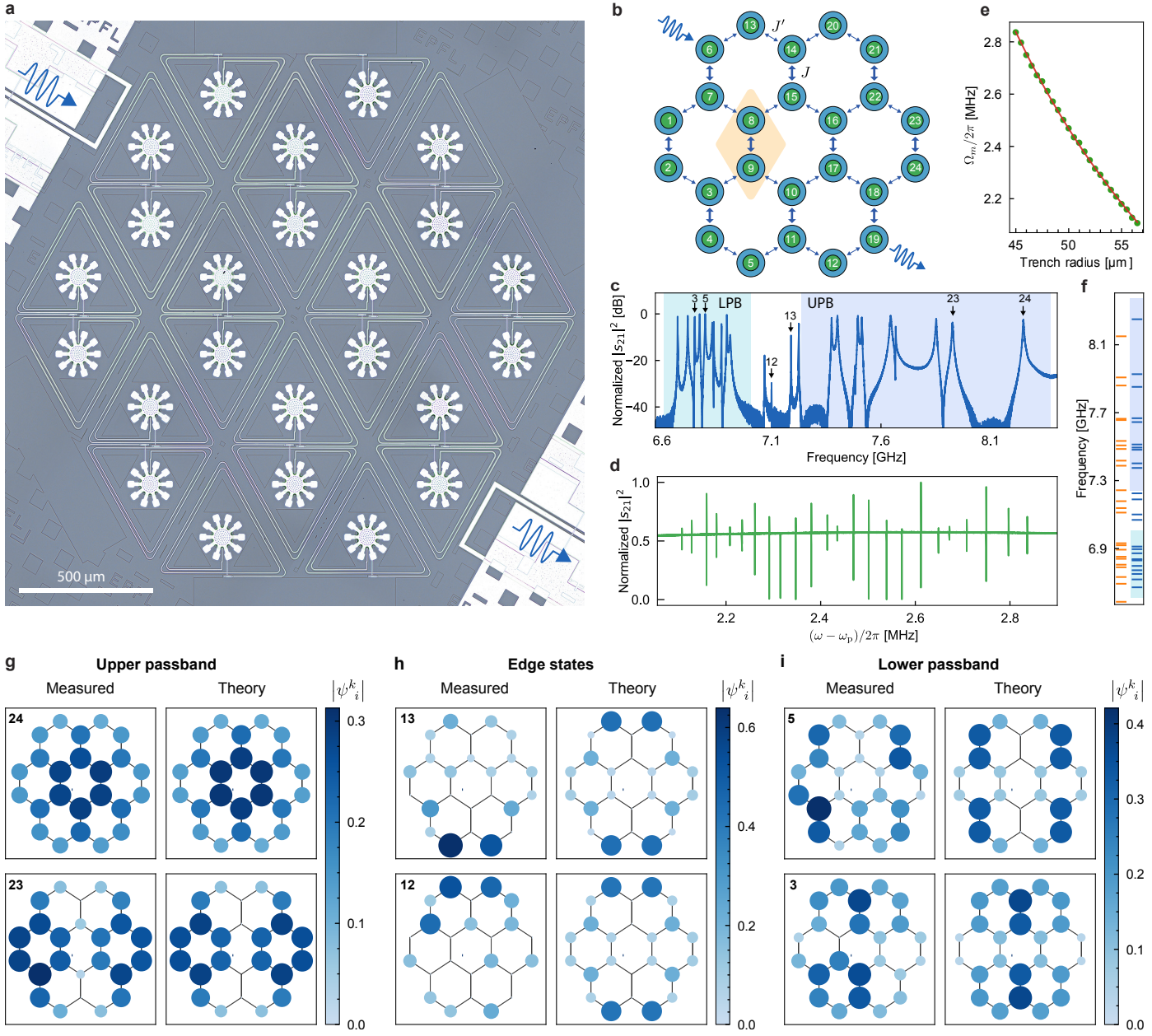


FIG. 4. Realization of a two-dimensional topological optomechanical honeycomb lattice. **a**, Optical micrograph of a 24 site honeycomb optomechanical lattice with alternating couplings. **b**, Mode diagram of the device shown in **a**. **c**, Transmission spectrum of the 2D lattice. Four topological edge modes are distinguished in the band gap. **d**, OMIT spectrum on the highest frequency collective mode. **e**, Measured mechanical frequencies versus trench radius and the inverse linear fit. **f**, Measured (blue) and design target (orange) microwave resonances. **g**, **h**, **i**, Examples of measured mode shapes of the 2D lattice in UPB, edge states, and LPB respectively. The mode shape information in amplitude is reflected on color and area of each circle.

constructed Hamiltonian of the 1D SSH device, in the rotating frame with the average cavity frequency. The diagonal elements represent the cavity frequency disorder of each site ($\sigma_{\Delta\omega} = 0.5\%$ corresponds to a 2 nm gap size variation), while off-diagonal elements show the alternating microwave couplings as designed for the SSH model and parasitic second and third nearest neighbor couplings between distanced sites.

Two-dimensional circuit optomechanical lattice

Two-dimensional superconducting lattices are attractive platforms for applications in many-body physics studies [67–69] and quantum simulation [70]. The platform introduced here can be straightforwardly extended to 2D structures. As a proof-of-concept experiment, we realized a 2D honeycomb optomechanical lattice. To

demonstrate the coupling tunability and inspired by the standard 1D SSH model, we choose to alternate the mutual microwave couplings (J and J') along the vertical axis (Fig. 4b). For such a system, the tight-binding model results in two separate bands (UPB and LPB) in the infinite case (see SI). In a finite lattice, similarly to the 1D SSH analog, topological edge states can arise under certain conditions ($J'/J < 2$) [71, 72].

Figure 4a shows a 24 site circuit optomechanical system, where the triangular spiral inductor in each site is inductively coupled to its three neighbors. The system is designed in the topological phase and supports four edge states in the bang gap (see SI for details). Figure 4c shows the transmission spectrum of the lattice. Figures 4d, and e show the OMIT response on the highest UPB mode and extracted mechanical frequencies versus trench radius correspondingly. We performed a full mode shape measurement on the 2D device, revealing close agreement to the theoretical calculations. A few examples of collective mode shapes in UPB, LPB, and topological edge states are shown in Fig. 4e,g,h (the full result can be found in the SI).

Conclusion and outlook

In summary, we realized optomechanical lattices demonstrating the SHH model in both 1D and 2D with exceptionally low disorder. Moreover, we demonstrated how the optomechanical interaction can be exploited for direct measurements of the Hamiltonian, beyond the tight binding approximation. Looking forward, such optomechanical lattices offer a path to realize proposals

exploring the rich physics in multimode optomechanics, ranging from quench [25] and collective [41] dynamics, to reservoir engineering [30]. Specifically, by using degenerate mechanical oscillators it is possible to create *collective* long-range interactions and observe strong coupling in optomechanical arrays [42], as well as quantum many-body dynamics [24]. Finally our system may enable the generation of highly entangled mechanical states [28], and viewed more broadly, it can be used to explore quantum correlations in topological optomechanical lattices [10, 24, 26, 27].

Data availability statement

The code and data used to produce the plots within this paper will be available at a Zenodo open-access repository. All other data used in this study are available from the corresponding authors upon reasonable request.

Acknowledgments

We thank T. Sugiyama for fruitful discussions. This work was supported by the EU H2020 research and innovation programme under grant No. 101033361 (QuPhon), and from the European Research Council (ERC) grant No. 835329 (ExCOM-cCEO). This work was also supported by the Swiss National Science Foundation (SNSF) under grant No. NCCR-QSIT: 51NF40_185902 and No. 182103. All devices were fabricated in the Center of MicroNanoTechnology (CMi) at EPFL.

* These authors contributed equally.

† tobias.kippenberg@epfl.ch

- [1] M. Aspelmeyer, T. J. Kippenberg, and F. Marquardt, Cavity optomechanics, *Reviews of Modern Physics* **86**, 1391 (2014).
- [2] T. J. Kippenberg and K. J. Vahala, Cavity optomechanics: back-action at the mesoscale, *science* **321**, 1172 (2008).
- [3] M. Aspelmeyer, P. Meystre, and K. Schwab, Quantum optomechanics, *Physics Today* **65**, 29 (2012).
- [4] S. Kotler, G. A. Peterson, E. Shojaee, F. Lecocq, K. Cicak, A. Kwiatkowski, S. Geller, S. Glancy, E. Knill, R. W. Simmonds, *et al.*, Direct observation of deterministic macroscopic entanglement, *Science* **372**, 622 (2021).
- [5] C. Ockeloen-Korppi, E. Damskägg, J.-M. Pirkkalainen, M. Asjad, A. Clerk, *et al.*, Stabilized entanglement of massive mechanical oscillators, *Nature* **556**, 478 (2018).
- [6] E. E. Wollman, C. Lei, A. Weinstein, J. Suh, A. Kronwald, F. Marquardt, A. A. Clerk, and K. Schwab, Quantum squeezing of motion in a mechanical resonator, *Science* **349**, 952 (2015).
- [7] A. H. Safavi-Naeini, J. Chan, J. T. Hill, T. P. M. Alegre, A. Krause, and O. Painter, Observation of quantum motion of a nanomechanical resonator, *Physical Review Letters* **108**, 033602 (2012).
- [8] N. R. Bernier, L. D. Tóth, A. Koottandavida, M. A. Ioannou, D. Malz, *et al.*, Nonreciprocal reconfigurable microwave optomechanical circuit, *Nature Communications* **8**, 10.1038/s41467-017-00447-1 (2017).
- [9] R. W. Andrews, R. W. Peterson, T. P. Purdy, K. Cicak, R. W. Simmonds, *et al.*, Bidirectional and efficient conversion between microwave and optical light, *Nature Physics* **10**, 321 (2014).
- [10] V. Peano, C. Brendel, M. Schmidt, and F. Marquardt, Topological phases of sound and light, *Physical Review X* **5**, 031011 (2015).
- [11] M. Mirhosseini, E. Kim, V. S. Ferreira, M. Kalaei, A. Sipahigil, A. J. Keller, and O. Painter, Superconducting metamaterials for waveguide quantum electrodynamics, *Nature communications* **9**, 1 (2018).
- [12] A. J. Kollár, M. Fitzpatrick, and A. A. Houck, Hyperbolic lattices in circuit quantum electrodynamics, *Nature* **571**, 45 (2019).
- [13] I. Carusotto, A. A. Houck, A. J. Kollár, P. Roushan, D. I. Schuster, and J. Simon, Photonic materials in circuit quantum electrodynamics, *Nature Physics* **16**, 268

(2020).

[14] C. W. Peterson, W. A. Benalcazar, T. L. Hughes, and G. Bahl, A quantized microwave quadrupole insulator with topologically protected corner states, *Nature* **555**, 346 (2018).

[15] J. D. Teufel, T. Donner, D. Li, J. W. Harlow, M. S. Allman, *et al.*, Sideband cooling of micromechanical motion to the quantum ground state, *Nature* **475**, 359–363 (2011).

[16] W. Su, J. Schrieffer, and A. J. Heeger, Solitons in polyacetylene, *Physical review letters* **42**, 1698 (1979).

[17] T. Ozawa, H. M. Price, A. Amo, N. Goldman, M. Hafezi, L. Lu, M. C. Rechtsman, D. Schuster, J. Simon, O. Zilbermanberg, *et al.*, Topological photonics, *Reviews of Modern Physics* **91**, 015006 (2019).

[18] J. K. Asbóth, L. Oroszlány, and A. Pályi, A short course on topological insulators, *Lecture notes in physics* **919**, 997 (2016).

[19] D. Underwood, W. Shanks, A. C. Li, L. Ateshian, J. Koch, and A. A. Houck, Imaging photon lattice states by scanning defect microscopy, *Physical Review X* **6**, 021044 (2016).

[20] M. Topinka, B. LeRoy, S. Shaw, E. Heller, R. Westervelt, K. Maranowski, and A. Gossard, Imaging coherent electron flow from a quantum point contact, *Science* **289**, 2323 (2000).

[21] M. Topinka, B. LeRoy, R. Westervelt, S. Shaw, R. Fleischmann, E. Heller, K. Maranowski, and A. Gossard, Coherent branched flow in a two-dimensional electron gas, *Nature* **410**, 183 (2001).

[22] H. Wang, A. Zhuravel, S. Indrajeet, B. G. Taketani, M. Hutchings, Y. Hao, F. Rouxinol, F. Wilhelm, M. LaHaye, A. Ustinov, *et al.*, Mode structure in superconducting metamaterial transmission-line resonators, *Physical Review Applied* **11**, 054062 (2019).

[23] A. Morvan, M. Féchant, G. Aiello, J. Gabelli, and J. Estève, Bulk properties of honeycomb lattices of superconducting microwave resonators, *arXiv preprint arXiv:2103.09428* (2021).

[24] M. Ludwig and F. Marquardt, Quantum many-body dynamics in optomechanical arrays, *Physical review letters* **111**, 073603 (2013).

[25] S. Raeisi and F. Marquardt, Quench dynamics in one-dimensional optomechanical arrays, *Physical Review A* **101**, 023814 (2020).

[26] F. Zangeneh-Nejad and R. Fleury, Topological optomechanically induced transparency, *Optics Letters* **45**, 5966 (2020).

[27] L. Qi, Y. Xing, H.-F. Wang, A.-D. Zhu, and S. Zhang, Simulating $z=2$ topological insulators via a one-dimensional cavity optomechanical cells array, *Optics express* **25**, 17948 (2017).

[28] U. Akram, W. Munro, K. Nemoto, and G. Milburn, Photon-phonon entanglement in coupled optomechanical arrays, *Physical Review A* **86**, 042306 (2012).

[29] C. Sanavio, V. Peano, and A. Xuereb, Nonreciprocal topological phononics in optomechanical arrays, *Physical Review B* **101**, 085108 (2020).

[30] A. Tomadin, S. Diehl, M. D. Lukin, P. Rabl, and P. Zoller, Reservoir engineering and dynamical phase transitions in optomechanical arrays, *Physical Review A* **86**, 033821 (2012).

[31] J.-H. Gan, H. Xiong, L.-G. Si, X.-Y. Lü, and Y. Wu, Solitons in optomechanical arrays, *Optics letters* **41**, 2676 (2016).

[32] J. Van Beek and R. Puers, A review of mems oscillators for frequency reference and timing applications, *Journal of Micromechanics and Microengineering* **22**, 013001 (2011).

[33] R. C. Ruby, P. Bradley, Y. Oshmyansky, A. Chien, and J. D. Larson, Thin film bulk wave acoustic resonators (fbars) for wireless applications, in *2001 IEEE Ultrasonics Symposium. Proceedings. An International Symposium (Cat. No. 01CH37263)*, Vol. 1 (IEEE, 2001) pp. 813–821.

[34] A. D. O’Connell, M. Hofheinz, M. Ansmann, R. C. Bialczak, M. Lenander, E. Lucero, M. Neeley, D. Sank, H. Wang, M. Weides, *et al.*, Quantum ground state and single-phonon control of a mechanical resonator, *Nature* **464**, 697 (2010).

[35] J. D. Teufel, T. Donner, M. Castellanos-Beltran, J. W. Harlow, and K. W. Lehnert, Nanomechanical motion measured with an imprecision below that at the standard quantum limit, *Nature nanotechnology* **4**, 820 (2009).

[36] G. Anetsberger, E. Gavartin, O. Arcizet, Q. P. Unterreithmeier, E. M. Weig, M. L. Gorodetsky, J. P. Kotthaus, and T. J. Kippenberg, Measuring nanomechanical motion with an imprecision below the standard quantum limit, *Physical Review A* **82**, 061804 (2010).

[37] J. D. Teufel, T. Donner, D. Li, J. W. Harlow, M. Allman, K. Cicak, A. J. Sirois, J. D. Whittaker, K. W. Lehnert, and R. W. Simmonds, Sideband cooling of micromechanical motion to the quantum ground state, *Nature* **475**, 359 (2011).

[38] J. Chan, T. M. Alegre, A. H. Safavi-Naeini, J. T. Hill, A. Krause, S. Gröblacher, M. Aspelmeyer, and O. Painter, Laser cooling of a nanomechanical oscillator into its quantum ground state, *Nature* **478**, 89 (2011).

[39] T. Palomaki, J. Harlow, J. Teufel, R. Simmonds, and K. W. Lehnert, Coherent state transfer between itinerant microwave fields and a mechanical oscillator, *Nature* **495**, 210 (2013).

[40] R. Riedinger, A. Wallucks, I. Marinković, C. Löschner, M. Aspelmeyer, S. Hong, and S. Gröblacher, Remote quantum entanglement between two micromechanical oscillators, *Nature* **556**, 473 (2018).

[41] G. Heinrich, M. Ludwig, J. Qian, B. Kubala, and F. Marquardt, Collective dynamics in optomechanical arrays, *Physical review letters* **107**, 043603 (2011).

[42] A. Xuereb, C. Genes, and A. Dantan, Strong coupling and long-range collective interactions in optomechanical arrays, *Physical review letters* **109**, 223601 (2012).

[43] T. F. Roque, V. Peano, O. M. Yevtushenko, and F. Marquardt, Anderson localization of composite excitations in disordered optomechanical arrays, *New Journal of Physics* **19**, 013006 (2017).

[44] A. H. Safavi-Naeini, J. T. Hill, S. Meenehan, J. Chan, S. Gröblacher, and O. Painter, Two-dimensional phononic-photonic band gap optomechanical crystal cavity, *Physical Review Letters* **112**, 153603 (2014).

[45] Z. Yang, F. Gao, X. Shi, X. Lin, Z. Gao, Y. Chong, and B. Zhang, Topological acoustics, *Physical review letters* **114**, 114301 (2015).

[46] S. D. Huber, Topological mechanics, *Nature Physics* **12**, 621 (2016).

[47] J. U. Surjadi, L. Gao, H. Du, X. Li, X. Xiong, N. X. Fang, and Y. Lu, Mechanical metamaterials and their engineering applications, *Advanced Engineering Materi-*

als **21**, 1800864 (2019).

[48] H. Ren, T. Shah, H. Pfeifer, C. Brendel, V. Peano, F. Marquardt, and O. Painter, Topological phonon transport in an optomechanical system, *arXiv* (2020).

[49] K. Cicak, D. Li, J. A. Strong, M. S. Allman, F. Altomare, A. J. Sirois, J. D. Whittaker, J. D. Teufel, and R. W. Simmonds, Low-loss superconducting resonant circuits using vacuum-gap-based microwave components, *Applied Physics Letters* **96**, 093502 (2010).

[50] L. M. de Lépinay, C. F. Ockeloen-Korppi, M. J. Woolley, and M. A. Sillanpää, Quantum mechanics-free subsystem with mechanical oscillators, *Science* **372**, 625 (2021).

[51] L. D. Tóth, N. R. Bernier, A. Nunnenkamp, A. K. Fedanov, and T. J. Kippenberg, A dissipative quantum reservoir for microwave light using a mechanical oscillator, *Nature Physics* **13**, 787–793 (2017).

[52] J.-M. Pirkkalainen, S. Cho, J. Li, G. Paraoanu, P. Hakonen, and M. Sillanpää, Hybrid circuit cavity quantum electrodynamics with a micromechanical resonator, *Nature* **494**, 211 (2013).

[53] A. Reed, K. Mayer, J. Teufel, L. Burkhart, W. Pfaff, M. Reagor, L. Sletten, X. Ma, R. Schoelkopf, E. Knill, *et al.*, Faithful conversion of propagating quantum information to mechanical motion, *Nature Physics* **13**, 1163 (2017).

[54] E. Kim, X. Zhang, V. S. Ferreira, J. Bunker, J. K. Iverson, A. Sipahigil, M. Bello, A. González-Tudela, M. Mirhosseini, and O. Painter, Quantum electrodynamics in a topological waveguide, *Physical Review X* **11**, 011015 (2021).

[55] I. Buluta and F. Nori, Quantum simulators, *Science* **326**, 108 (2009).

[56] A. A. Houck, H. E. Türeci, and J. Koch, On-chip quantum simulation with superconducting circuits, *Nature Physics* **8**, 292 (2012).

[57] D. L. Underwood, W. E. Shanks, J. Koch, and A. A. Houck, Low-disorder microwave cavity lattices for quantum simulation with photons, *Physical Review A* **86**, 023837 (2012).

[58] X. Gu, A. F. Kockum, A. Miranowicz, Y.-x. Liu, and F. Nori, Microwave photonics with superconducting quantum circuits, *Physics Reports* **718**, 1 (2017).

[59] B. Pérez-González, M. Bello, Á. Gómez-León, and G. Platero, Interplay between long-range hopping and disorder in topological systems, *Physical Review B* **99**, 035146 (2019).

[60] F. Massel, S. U. Cho, J.-M. Pirkkalainen, P. J. Hakonen, T. T. Heikkilä, and M. A. Sillanpää, Multimode circuit optomechanics near the quantum limit, *Nature communications* **3**, 1 (2012).

[61] A. Youssefi *et al.*, An ultra coherent circuit optomechanical quantum memory, in preparation.

[62] L. Li, Z. Xu, and S. Chen, Topological phases of generalized su-schrieffer-heeger models, *Physical Review B* **89**, 085111 (2014).

[63] B. Pérez-González, M. Bello, Á. Gómez-León, and G. Platero, Ssh model with long-range hoppings: topology, driving and disorder, *arXiv preprint arXiv:1802.03973* (2018).

[64] S. Weis, R. Riviere, S. Deleglise, E. Gavartin, O. Arcizet, *et al.*, Optomechanically induced transparency, *Science* **330**, 1520–1523 (2010).

[65] A. H. Safavi-Naeini, T. M. Alegre, J. Chan, M. Eichenfield, M. Winger, *et al.*, Electromagnetically induced transparency and slow light with optomechanics, *Nature* **472**, 69 (2011).

[66] P. St-Jean, V. Goblot, E. Galopin, A. Lemaître, T. Ozawa, L. Le Gratiet, I. Sagnes, J. Bloch, and A. Amo, Lasing in topological edge states of a one-dimensional lattice, *Nature Photonics* **11**, 651 (2017).

[67] J. Koch and K. Le Hur, Superfluid–mott-insulator transition of light in the jaynes-cummings lattice, *Physical Review A* **80**, 023811 (2009).

[68] J. Koch, A. A. Houck, K. Le Hur, and S. Girvin, Time-reversal-symmetry breaking in circuit-qed-based photon lattices, *Physical Review A* **82**, 043811 (2010).

[69] B. M. Anderson, R. Ma, C. Owens, D. I. Schuster, and J. Simon, Engineering topological many-body materials in microwave cavity arrays, *Physical Review X* **6**, 041043 (2016).

[70] S. Schmidt and J. Koch, Circuit qed lattices: towards quantum simulation with superconducting circuits, *Annalen der Physik* **525**, 395 (2013).

[71] Y. Hasegawa and M. Kohmoto, Quantum hall effect and the topological number in graphene, *Physical Review B* **74**, 155415 (2006).

[72] Y.-H. Li and R. Cheng, Magnonic su-schrieffer-heeger model in honeycomb ferromagnets, *Physical Review B* **103**, 014407 (2021).

Supplementary Information

Contents

References	7
1. Theory of multi-mode circuit optomechanics	11
A. Theoretical model	11
B. Extraction of participation ratio from optomechanical damping rate	13
C. Hamiltonian reconstruction	14
2. Circuit theory of the dimerized SSH arrays	15
3. Numerical analysis	16
A. Disorder effect and edge state hybridization in SSH chains	16
B. SSH model with second nearest neighbor coupling and beyond	18
C. Statistical analysis of orthogonality and measurement error	19
4. Two dimensional honeycomb lattice	19
A. Bulk Hamiltonian and Band Structure	20
B. Representation on the Bloch Sphere	21
C. Topological phase transition	21
D. Design of the 24 site honeycomb lattice	22
5. Design and simulation	22
A. Design principles	22
B. Electromagnetic simulations	23
6. Nanofabrication techniques	24
A. Challenges and limitations of the conventional fabrication process	24
B. The new reproducible nanofabrication process for circuit optomechanics	25
7. Experimental setup and measurement techniques	27
A. Full experimental setup	27
B. Ringdown data analysis and cavity shifts	28
C. Mode shape extraction methods comparison	29
8. Experimental observation of edge state localization	29
9. Full device characterisations	30
A. Samples parameters	30
B. Measurement of optomechanical coupling rate	31
C. 2D modeshapes and Hamiltonian reconstruction	33
References	36

Supplementary Note 1. Theory of multi-mode circuit optomechanics

A. Theoretical model

This section provides the theoretical description of a multi-mode circuit optomechanical system. In our model, each electromechanical element consists of a single microwave mode optomechanically coupled to an individual mechanical mode. In addition, the microwave modes are electromagnetically coupled to each other. The Hamiltonian of the multi-mode system is in general given by

$$\hat{H}/\hbar = \sum_i \left[\omega_{c,i} \hat{a}_i^\dagger \hat{a}_i + \Omega_{m,i} \hat{b}_i^\dagger \hat{b}_i + g_{0,i} \hat{a}_i^\dagger \hat{a}_i (\hat{b}_i^\dagger + \hat{b}_i) \right] + \sum_{i \neq j} (J_{ij} \hat{a}_i^\dagger \hat{a}_j + J_{ji} \hat{a}_j^\dagger \hat{a}_i), \quad (1)$$

where \hat{a}_i and \hat{b}_i are annihilation operators for microwave mode i with a resonance frequency $\omega_{c,i}$ and mechanical mode i with a resonance frequency $\Omega_{m,i}$, $g_{0,i}$ is the single-photon optomechanical coupling rate, and J_{ij} is the coupling strength between microwave modes i and j .

Assuming that the single-photon optomechanical coupling rates are sufficiently smaller than the microwave resonance frequencies and the electromagnetic coupling strengths, collective microwave modes can be well defined regardless of the coupling to the mechanical modes. Thus, we first focus on the Hamiltonian of the coupled microwave modes:

$$\hat{H}_c/\hbar = \sum_i \omega_{c,i} \hat{a}_i^\dagger \hat{a}_i + \sum_{i \neq j} (J_{ij} \hat{a}_i^\dagger \hat{a}_j + J_{ji} \hat{a}_j^\dagger \hat{a}_i). \quad (2)$$

In a matrix representation, the quadratic Hamiltonian \hat{H}_c can be described as

$$\hat{H}_c = \hat{\mathbf{a}}^\dagger \mathbf{H}_c \hat{\mathbf{a}}, \quad (3)$$

where

$$\hat{\mathbf{a}} = \begin{bmatrix} \hat{a}_1 \\ \hat{a}_2 \\ \vdots \\ \hat{a}_i \\ \vdots \end{bmatrix}, \quad \hat{\mathbf{a}}^\dagger = [\hat{a}_1^\dagger \ \hat{a}_2^\dagger \ \dots \ \hat{a}_i^\dagger \ \dots], \quad \text{and} \quad \mathbf{H}_c/\hbar = \begin{bmatrix} \ddots & & & \\ & \omega_{c,i} & & J_{ji} \\ & & \ddots & \\ J_{ij} & & \omega_{c,j} & \ddots \end{bmatrix}. \quad (4)$$

Since \mathbf{H}_c is an hermitian matrix, it can be diagonalized by a unitary matrix \mathbf{U}_ψ as

$$\mathbf{D}_c = \mathbf{U}_\psi \mathbf{H}_c \mathbf{U}_\psi^\dagger, \quad (5)$$

where \mathbf{D}_c is a diagonal matrix whose diagonal element $[\mathbf{D}_c]_{k,k}$ corresponds to the eigenenergy $\hbar\tilde{\omega}_c^k$ of collective microwave mode k . On the basis of the collective microwave modes $\hat{\mathbf{a}} = \mathbf{U}_\psi \hat{\mathbf{a}}$, Hamiltonian (2) is described as

$$\begin{aligned} \hat{H}_c/\hbar &= \hat{\mathbf{a}}^\dagger (\mathbf{D}_c/\hbar) \hat{\mathbf{a}} \\ &= \sum_k \tilde{\omega}_c^k \hat{a}_k^\dagger \hat{a}_k. \end{aligned} \quad (6)$$

Note that collective microwave mode k is explicitly represented using the bare microwave modes as

$$\hat{a}_k = \sum_i \psi_i^k \hat{a}_i, \quad (7)$$

where $\psi_i^k = [\mathbf{U}_\psi]_{k,i}$ is the complex amplitude of the normalized mode function of collective microwave mode k . Thus, we define the participation ratio of bare mode i to collective mode k as

$$\eta_i^k = |\psi_i^k|^2. \quad (8)$$

As discussed in the main text, our main goal is to characterize the participation ratio using the optomechanical damping effects in multi-mode optomechanics.

The property of the unitary transformation gives the normalization conditions of the mode functions:

$$\sum_i \eta_i^k = \sum_i |\psi_i^k|^2 = 1 \quad (9)$$

and

$$\sum_k \eta_i^k = \sum_k |\psi_i^k|^2 = 1, \quad (10)$$

as well as the orthogonalization condition between different mode functions:

$$\sum_i \psi_i^k * \psi_i^l = 0 \quad (\text{if } l \neq k). \quad (11)$$

The normalization condition of Eq. (9) describes the photon-number conservation in collective mode k when it is decomposed into the bare modes, while the normalization condition of Eq. (10) describes the photon-number conservation in bare mode i when it is decomposed into the collective modes.

Next, we describe the Hamiltonian of the multi-mode optomechanical system based on the collective microwave modes. Using the inverse unitary transformation $\hat{\mathbf{a}} = \mathbf{U}_\psi^\dagger \hat{\mathbf{a}}$, the bare microwave mode i is represented as

$$\hat{a}_i = \sum_k \psi_i^k * \hat{a}_k. \quad (12)$$

With this relation, Hamiltonian (1) is rewritten as

$$\hat{H}/\hbar = \sum_k \tilde{\omega}_c^k \hat{a}_k^\dagger \hat{a}_k + \sum_i \Omega_{m,i} \hat{b}_i^\dagger \hat{b}_i + \sum_{k,l,i} \left[g_{0,i} \psi_i^l * \psi_i^k \hat{a}_k^\dagger \hat{a}_l (\hat{b}_i^\dagger + \hat{b}_i) \right]. \quad (13)$$

Assuming that the frequency detuning among the collective microwave modes are sufficiently larger than the single-photon optomechanical coupling rate, the rotating-wave approximation can be valid, neglecting the non-energy conservation term $\propto \hat{a}_k^\dagger \hat{a}_l$ (if $k \neq l$). Thus, the Hamiltonian can be approximated as

$$\begin{aligned} \hat{H}/\hbar &= \sum_k \tilde{\omega}_c^k \hat{a}_k^\dagger \hat{a}_k + \sum_i \Omega_{m,i} \hat{b}_i^\dagger \hat{b}_i + \sum_{k,i} g_{0,i} \psi_i^k * \psi_i^k \hat{a}_k^\dagger \hat{a}_k (\hat{b}_i^\dagger + \hat{b}_i) \\ &= \sum_k \tilde{\omega}_c^k \hat{a}_k^\dagger \hat{a}_k + \sum_i \Omega_{m,i} \hat{b}_i^\dagger \hat{b}_i + \sum_{k,i} (\eta_i^k g_{0,i}) \hat{a}_k^\dagger \hat{a}_k (\hat{b}_i^\dagger + \hat{b}_i). \end{aligned} \quad (14)$$

In the collective-mode picture, mechanical mode i is optomechanically coupled to collective microwave mode k with the single-photon optomechanical coupling rate $g_{0,i}$ weighted by η_i^k , the participation ratio of bare microwave mode i to collective microwave mode k .

In our multi-mode optomechanical system, it can be assumed that the collective microwave modes and the mechanical modes are well isolated from each other in frequency space, enabling us to operate the multi-mode system as a single microwave mode coupled to a single mechanical mode. Furthermore, our multi-mode system is locally connected to an input line on one side and an output line on the other side, resulting in collective microwave mode k being coupled to the input line with the external coupling rate κ_1^k and the output line with the external coupling rate κ_2^k , respectively. Note that κ_1^k and κ_2^k depends on the mode function of collective mode k .

Here, we consider the case when collective microwave mode k is driven by a coherent field with a frequency ω_i^k from the input line to couple mechanical mode i to collective microwave mode k . The effective Hamiltonian in the rotating frame of ω_i^k is given by

$$\hat{H}_i^k/\hbar = \Delta_i^k \hat{a}_k^\dagger \hat{a}_k + \Omega_{m,i} \hat{b}_i^\dagger \hat{b}_i + (\eta_i^k g_{0,i}) \hat{a}_k^\dagger \hat{a}_k (\hat{b}_i^\dagger + \hat{b}_i) + \sqrt{\kappa_1^k n_d^k} (\hat{a}_k^\dagger + \hat{a}_k), \quad (15)$$

where $\Delta_i^k = \tilde{\omega}_c^k - \omega_i^k$ is the detuning between the collective microwave frequency $\tilde{\omega}_c^k$ and the drive frequency ω_i^k and n_d^k is the photon flux of the cavity drive field. With this Hamiltonian, the quantum Langevin equations of collective microwave mode k and mechanical mode i are given by

$$\begin{aligned} \dot{\hat{a}}_k &= \left[-i\Delta_i^k - \frac{\kappa_{\text{tot}}^k}{2} - i(\eta_i^k g_{0,i}) (\hat{b}_i^\dagger + \hat{b}_i) \right] \hat{a}_k - i\sqrt{\kappa_1^k n_d^k} + \sqrt{\kappa_1^k} \hat{a}_{\text{in},1} + \sqrt{\kappa_2^k} \hat{a}_{\text{in},2} + \sqrt{\kappa_0^k} \hat{a}_{\text{in},0} \\ \dot{\hat{b}}_i &= \left(-i\Omega_{m,i} - \frac{\Gamma_{m,i}}{2} \right) \hat{b}_i - i(\eta_i^k g_{0,i}) \hat{a}_k^\dagger \hat{a}_k + \sqrt{\Gamma_{m,i}} \hat{b}_{\text{in}}, \end{aligned} \quad (16)$$

where κ_0^k and $\kappa_{\text{tot}}^k = \kappa_0^k + \kappa_1^k + \kappa_2^k$ are the intrinsic loss rate and the total decay rate of the microwave mode, respectively. Moreover, $\Gamma_{\text{m},i}$ is the intrinsic loss rate of the mechanical mode, and $\hat{a}_{\text{in},0}$, $\hat{a}_{\text{in},1}$, $\hat{a}_{\text{in},2}$, are \hat{b}_{in} are input quantum noises from the corresponding baths.

Assuming that the coherent amplitude of the microwave mode is not affected by the optomechanical coupling, the Langevin equation for the microwave mode can be divided into the classical part with $\langle \hat{\alpha}_k \rangle$ and the quantum part with $\delta\hat{\alpha}_k$. By using the linearization $\hat{\alpha}_k = \langle \hat{\alpha}_k \rangle + \delta\hat{\alpha}_k$, we therefore have

$$\begin{aligned}\langle \dot{\hat{\alpha}}_k \rangle &= \left(-i\Delta_i^k - \frac{\kappa_{\text{tot}}^k}{2} \right) \langle \hat{\alpha}_k \rangle - i\sqrt{\kappa_1^k n_{\text{d}}^k} \\ \dot{\delta\hat{\alpha}}_k &= \left(-i\Delta_i^k - \frac{\kappa_{\text{tot}}^k}{2} \right) \delta\hat{\alpha}_k - i(\eta_i^k g_{0,i}) \langle \hat{\alpha}_k \rangle (\hat{b}_i^\dagger + \hat{b}_i) + \sqrt{\kappa_1^k} \hat{a}_{\text{in},1} + \sqrt{\kappa_2^k} \hat{a}_{\text{in},2} + \sqrt{\kappa_0^k} \hat{a}_{\text{in},0} \\ \dot{\hat{b}}_i &= \left(-i\Omega_{\text{m},i} - \frac{\Gamma_{\text{m},i}}{2} \right) \hat{b}_i - i(\eta_i^k g_{0,i}) (\langle \hat{\alpha}_k \rangle \hat{a}_k^\dagger + \langle \hat{\alpha}_k \rangle^* \hat{\alpha}_k) + \sqrt{\Gamma_{\text{m},i}} \hat{b}_{\text{in}}.\end{aligned}\quad (17)$$

Note that the bare optomechanical coupling terms are neglected. The time evolution of the mechanical mode is sufficiently slow for the classical amplitude of the microwave mode to be in the steady state. Using $\langle \dot{\hat{\alpha}}_k \rangle = 0$, the classical amplitude is therefore obtained as

$$\langle \hat{\alpha}_k \rangle = \frac{-i\sqrt{\kappa_1^k n_{\text{d}}^k}}{i\Delta_i^k + \frac{\kappa_{\text{tot}}^k}{2}}. \quad (18)$$

B. Extraction of participation ratio from optomechanical damping rate

As discussed in the main text, we characterize the participation ratio η_i^k by measuring the optomechanical damping rate of mechanical mode i coupled to collective mode k . From Eqs. (17), the optomechanical damping rate [1] is given by

$$\Gamma_{\text{opt},i}^k = n_{\text{c},i}^k (\eta_i^k g_{0,i})^2 \left(\frac{\kappa_{\text{tot}}^k}{(\Omega_{\text{m},i} - \Delta_i^k)^2 + \kappa_{\text{tot}}^k/4} - \frac{\kappa_{\text{tot}}^k}{(\Omega_{\text{m},i} + \Delta_i^k)^2 + \kappa_{\text{tot}}^k/4} \right), \quad (19)$$

where

$$n_{\text{c},i}^k = |\langle \hat{\alpha}_k \rangle|^2 = \frac{n_{\text{d}}^k \kappa_1^k}{\Delta_i^{k^2} + \kappa_{\text{tot}}^k/4}$$

is the average photon number in collective mode k , where n_{d}^k is the on-chip photon flux. This yields the total effective damping rate of mechanical mode i :

$$\Gamma_{\text{eff},i}^k = \Gamma_{\text{m},i} + \Gamma_{\text{opt},i}^k. \quad (20)$$

To extract the optomechanical damping effect, we linearly change the drive power generated by a microwave source. Here, we define the transmittance between the microwave source and the device as $R^k = n_{\text{d}}^k/n_{\text{d}}$, where n_{d} is the photon flux at the output of the microwave source. Note that we assume that the frequency dependence of the transmittance can be negligible when the different mechanical modes are coupled to collective microwave mode k by the drive field. Then, we obtain $\partial\Gamma_{\text{eff},i}^k/\partial n_{\text{d}}$, the slope of the total damping rate with respect to the photon flux n_{d} .

From Eq. (19), the slope of the total mechanical damping rate is analytically obtained as

$$\frac{\partial\Gamma_{\text{eff},i}^k}{\partial n_{\text{d}}} = \frac{\kappa_1^k R^k (\eta_i^k g_{0,i})^2}{\Delta_i^{k^2} + \kappa_{\text{tot}}^k/4} \left(\frac{\kappa_{\text{tot}}^k}{(\Omega_{\text{m},i} - \Delta_i^k)^2 + \kappa_{\text{tot}}^k/4} - \frac{\kappa_{\text{tot}}^k}{(\Omega_{\text{m},i} + \Delta_i^k)^2 + \kappa_{\text{tot}}^k/4} \right). \quad (21)$$

From this equation, we experimentally obtain the unnormalized participation ratio as

$$\widetilde{\eta_i^k} = \sqrt{\frac{\partial\Gamma_{\text{eff},i}^k}{\partial n_{\text{d}}} (\Delta_i^{k^2} + \kappa_{\text{tot}}^k/4) \left(\frac{\kappa_{\text{tot}}^k}{(\Omega_{\text{m},i} - \Delta_i^k)^2 + \kappa_{\text{tot}}^k/4} - \frac{\kappa_{\text{tot}}^k}{(\Omega_{\text{m},i} + \Delta_i^k)^2 + \kappa_{\text{tot}}^k/4} \right)^{-1}}. \quad (22)$$

By definitions in Eqs. (21) and (22), the relation between the normalized and unnormalized participation ratios is described as

$$\widetilde{\eta}_i^k = g_{0,i} \eta_i^k \sqrt{\kappa_1^k R^k}. \quad (23)$$

In principle, the normalized participation ratio η_i^k can be determined by using $g_{0,i}$, κ_1^k and R^k that would be obtained independently. However, the local optomechanical coupling $g_{0,i}$ can not be straightforwardly measured in such a multimode optomechanical system. Furthermore, it is also not trivial to determine κ_1^k and R^k using our setup in a transmission configuration.

Nevertheless, we can determine η_i^k from experimentally-obtainable $\widetilde{\eta}_i^k$ based on the normalization conditions of the unitary transformation [Eqs. (9) and (10)]. Here, we apply an iterative normalization method for $\widetilde{\eta}_i^k$ as follows. We first define the initial unnormalized participation ratio as

$$\widetilde{\eta}_i^k(0) = \widetilde{\eta}_i^k. \quad (24)$$

Then, we iterate the normalization process in the row and column axes alternatively. Namely, the unnormalized participation ratio $\widetilde{\eta}_i^k(n)$ is updated in each normalization step to $\widetilde{\eta}_i^k(n+1)$ as

$$\widetilde{\eta}_i^k(n+1) = \frac{\widetilde{\eta}_i^k(n)}{\sum_i \widetilde{\eta}_i^k(n)} \quad (\forall k, \text{ if } n \text{ is even}). \quad (25)$$

or

$$\widetilde{\eta}_i^k(n+1) = \frac{\widetilde{\eta}_i^k(n)}{\sum_k \widetilde{\eta}_i^k(n)} \quad (\forall i, \text{ if } n \text{ is odd}). \quad (26)$$

In the iterative normalization method, the unnormalized participation ratio at step n can be always described as

$$\widetilde{\eta}_i^k(n) = C_{i(n)} \eta_i^k D_{k(n)}, \quad (27)$$

where $C_{i(n)}$ and $D_{k(n)}$ are coefficients depending only on either i or k . Importantly, each normalization process updates only these coefficients without any changes in η_i^k . We numerically confirm that both $C_{i(n)}$ and $D_{k(n)}$ converge to 1 with a sufficiently large number of the iteration. Thus, even without knowledge of the coefficients, the initial participation ratio converges to the normalized one, i.e. $\widetilde{\eta}_i^k(n) \rightarrow \eta_i^k$ when $n \rightarrow \infty$. Empirically, $n = 50$ is sufficient for $\widetilde{\eta}_i^k$ to converge to η_i^k .

C. Hamiltonian reconstruction

Considering the knowledge of all the eigenvectors \mathbf{U}_ψ and eigenvalues \mathbf{D}_c of the system, we can reconstruct the actual Hamiltonian of the system using Eq. (5):

$$\mathbf{H}_c = \mathbf{U}_\psi^\dagger \mathbf{D}_c \mathbf{U}_\psi. \quad (28)$$

The diagonal matrix of the eigenvalues \mathbf{D}_c can be straightforwardly determined from the transmission spectrum of the multi-mode system. However, our measurement scheme does not retrieve the sign of the mode shapes of the collective microwave modes to fully determine the unitary matrix \mathbf{U}_ψ . By inferring the phase information from the theoretical mode shapes calculated in Sec. 3B, we can construct the “unitary” matrix $\widetilde{\mathbf{U}}_\psi$ from η_i^k that is obtained by the iterative normalization method, i.e.

$$[\widetilde{\mathbf{U}}_\psi]_{k,i} = +\sqrt{\eta_i^k} \quad \text{or} \quad -\sqrt{\eta_i^k}. \quad (29)$$

While it satisfies the normalization conditions in Eqs. (9) and (10), the obtained matrix does not satisfy the orthogonalization condition in Eq. (11) due to the finite measurement error in the participation ratio. To more accurately

reconstruct the Hamiltonian, we further correct $\tilde{\mathbf{U}}_\psi$ to satisfy both the normalization and orthogonalization conditions. We first numerically calculate the generator of $\tilde{\mathbf{U}}_\psi$ as

$$\mathbf{G} = \log(\tilde{\mathbf{U}}_\psi). \quad (30)$$

In general, the matrix can be decomposed into a Hermitian matrix \mathbf{H} and anti-Hermitian matrix $\bar{\mathbf{H}}$ as

$$\mathbf{G} = \mathbf{H} + \bar{\mathbf{H}}, \quad (31)$$

where $\mathbf{H} = (\mathbf{G} + \mathbf{G}^\dagger)/2$ and $\bar{\mathbf{H}} = (\mathbf{G} - \mathbf{G}^\dagger)/2i$. Although the generator of a unitary matrix only contains an anti-Hermitian matrix, the experimentally obtained \mathbf{G} contains the finite Hermitian component. By neglecting the Hermitian component, the corrected unitary matrix can be obtained as

$$\mathbf{U}_\psi = \exp(\bar{\mathbf{H}}). \quad (32)$$

Using the corrected unitary matrix together with Eq. (28), we reconstruct the Hamiltonian of the microwave subsystem, shown in Fig. 3f in the main text and Fig. 21 in SI.

Supplementary Note 2. Circuit theory of the dimerized SSH arrays

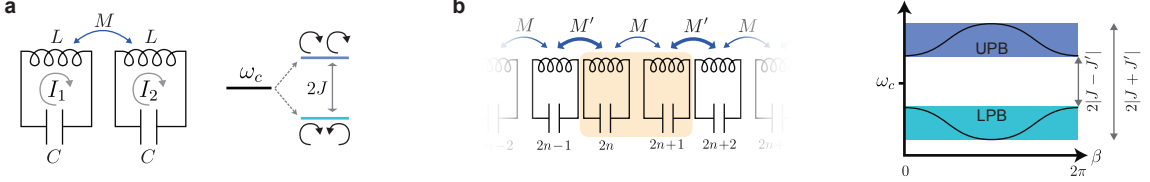


FIG. 1. **Circuit theory of the dimerized arrays.** **a**, Two coupled LC circuits. The inductive coupling results in energy splitting. The higher frequency mode supports symmetric currents. **b**, Infinite chain of dimerized circuits. The energy band structure consists of two passbands (UPB and LPB).

Here we briefly discuss the circuit theory of microwave SSH chains and link the circuit elements of such a system to the Hamiltonian parameters. We first consider two coupled identical LC circuits as shown in figure 1a. The system can be described by electrical currents, $I_1(t)$ and $I_2(t)$. Kirchhoff's equations result in:

$$L\ddot{I}_1(t) - M\ddot{I}_2(t) + \frac{1}{C}I_1(t) = 0, \quad L\ddot{I}_2(t) - M\ddot{I}_1(t) + \frac{1}{C}I_2(t) = 0 \quad (33)$$

Which can be transferred to the frequency domain:

$$(\omega_c^2 - \omega^2)L I_1 = -M\omega^2 I_2, \quad (\omega_c^2 - \omega^2)L I_2 = -M\omega^2 I_1 \quad (34)$$

Where $\omega_c = \sqrt{\frac{1}{LC}}$. Equation 34 results in two eigenfrequencies

$$\omega_c \sqrt{\frac{1}{1 \mp \frac{M}{L}}} \simeq \omega_c \left(1 \pm \frac{M}{2L}\right) \quad (35)$$

corresponding to two eigen modes of $I_1 = \pm I_2$ respectively. Based on the energy splitting, the energy coupling rate can be extracted as $J = \omega_c \frac{M}{2L}$. It is worth to mention that the symmetric mode ($I_1 = I_2$) corresponds to the higher resonance frequency and the asymmetric mode to the lower one.

Now we describe the infinite array of coupled dimer LC circuits with the staggered couplings of M and M' as shown in figure 1b. For each dimer (sites $2n$ and $2n+1$) we can derive the frequency domain circuit equations:

$$\begin{aligned} (\omega_c^2 - \omega_2)I_{2n} + \frac{M}{L}\omega^2 I_{2n+1} + \frac{M'}{L}\omega^2 I_{2(n-1)+1} &= 0 \\ (\omega_c^2 - \omega_2)I_{2n+1} + \frac{M'}{L}\omega^2 I_{2(n+1)} + \frac{M}{L}\omega^2 I_{2n} &= 0. \end{aligned} \quad (36)$$

Considering Bloch's theorem, the propagating mode in such array can be described by a harmonic function:

$$I_{2n} = e^{i\beta 2n} \quad , \quad I_{2n+1} = \lambda e^{i\beta 2n} \quad (37)$$

Where $\beta \in \mathbb{R}$ is the wave number of the propagating mode, and $\lambda \in \mathbb{C}$ is defining the phase and amplitude difference between circuits in a dimer. Therefore equation 36 will be simplified to:

$$\begin{aligned} (\omega_c^2 - \omega^2) + \lambda \frac{M + M' e^{-i\beta}}{L} \omega^2 &= 0 \\ \lambda(\omega_c^2 - \omega^2) + \frac{M + M' e^{i\beta}}{L} \omega^2 &= 0 \quad . \end{aligned} \quad (38)$$

Solving for ω from equations 38 will result in the band structure of the infinite chain:

$$\omega = \frac{\omega_c}{\sqrt{1 \pm \frac{\sqrt{M^2 + M'^2 + 2MM' \cos(\beta)}}{L}}} \quad . \quad (39)$$

As shown in figure 1b, the energy spectrum of the infinite chain consists of two passbands. In case of small mutual coupling ($\frac{M}{L}, \frac{M'}{L} \ll 1$) The upper passband (UPB) and lower passband boundaries are:

$$\begin{aligned} \omega_{\pm}^{\text{UPB}} &= \omega_c + |J \pm J'| \\ \omega_{\pm}^{\text{LPB}} &= \omega_c - |J \mp J'| \end{aligned} \quad (40)$$

Where $J = \omega_c \frac{M}{2L}$, $J' = \omega_c \frac{M'}{2L}$ are the mutual coupling rates in the chain. In the finite chains, when $J < J'$, two edge states arise in the middle of the bandgap due to the truncated boundary condition of the chain. This can be intuitively understood in the extreme case of $J \ll J'$, when the first and last LC circuits are fully isolated from the rest of the chain, which consists of strongly coupled circuits.

Supplementary Note 3. Numerical analysis

A. Disorder effect and edge state hybridization in SSH chains

Here we discuss the effect of disorder in the finite SSH chains. In any realized system, disorder and fluctuations can distort the system's parameters and consequently deviate the response from the ideal model. There are two possible types of disorder in the coupled circuit chains: cavity frequency fluctuation and mutual coupling rate fluctuation. In the case of electromechanical arrays introduced in this work, the coupling rate fluctuation is related to the -lithographically defined- self and mutual inductances disorder. In contrast to capacitive coupling where the coupling rate depends on the local electric field between closely spaces electrodes, here the coupling rate depends on the longer-range magnetic field generated by spirals and is more robust to the geometry distortions that arise from the lithographic accuracy (~ 500 nm). The dominant source of disorder is the capacitor's gap size fluctuation, which is strongly depending on CMP planarization uniformity as well as the etched trench depth variation. The gap size fluctuation was observed up to 1% using mechanical profilometry (which corresponds to 0.5% cavity frequency fluctuation).

To study the effect of disorder on the energy spectrum and mode structure of the SSH chains, here we consider a stochastic error on the cavity frequencies with normal distribution:

$$\omega_{c,i} = \omega_c (1 + \mathcal{N}(0, \sigma_{\Delta\omega})) \quad (41)$$

Where \mathcal{N} is a Gaussian stochastic variable and $\sigma_{\Delta\omega}$ is the relative cavity frequency error. Assuming coupling rates and resonance frequencies same as the 10 cell SSH chain discussed in the main text, we numerically calculate the energy spectrum and mode shapes for various relative disorder standard deviations, $\sigma_{\Delta\omega}$. Figure 2a shows the result for frequency disorder up to 6%, averaged over 4000 random distributions for each standard deviation. The uncertainty (\pm standard deviation) in energies increases with the disorder as shown with shaded areas in figure 2a and leads to the regime that two eigenmodes are not distinguishable anymore, as they overlap. As mentioned in the main text, the ideal SSH model in finite chains always results in two topological edge states, both with co-localized mode shapes on two edges regardless of the size of the chain (See figure 1h in the main text). In contrast to eigen energies that are robust against disorder, the topological mode shapes hybridization will break down sooner due to disorder and result

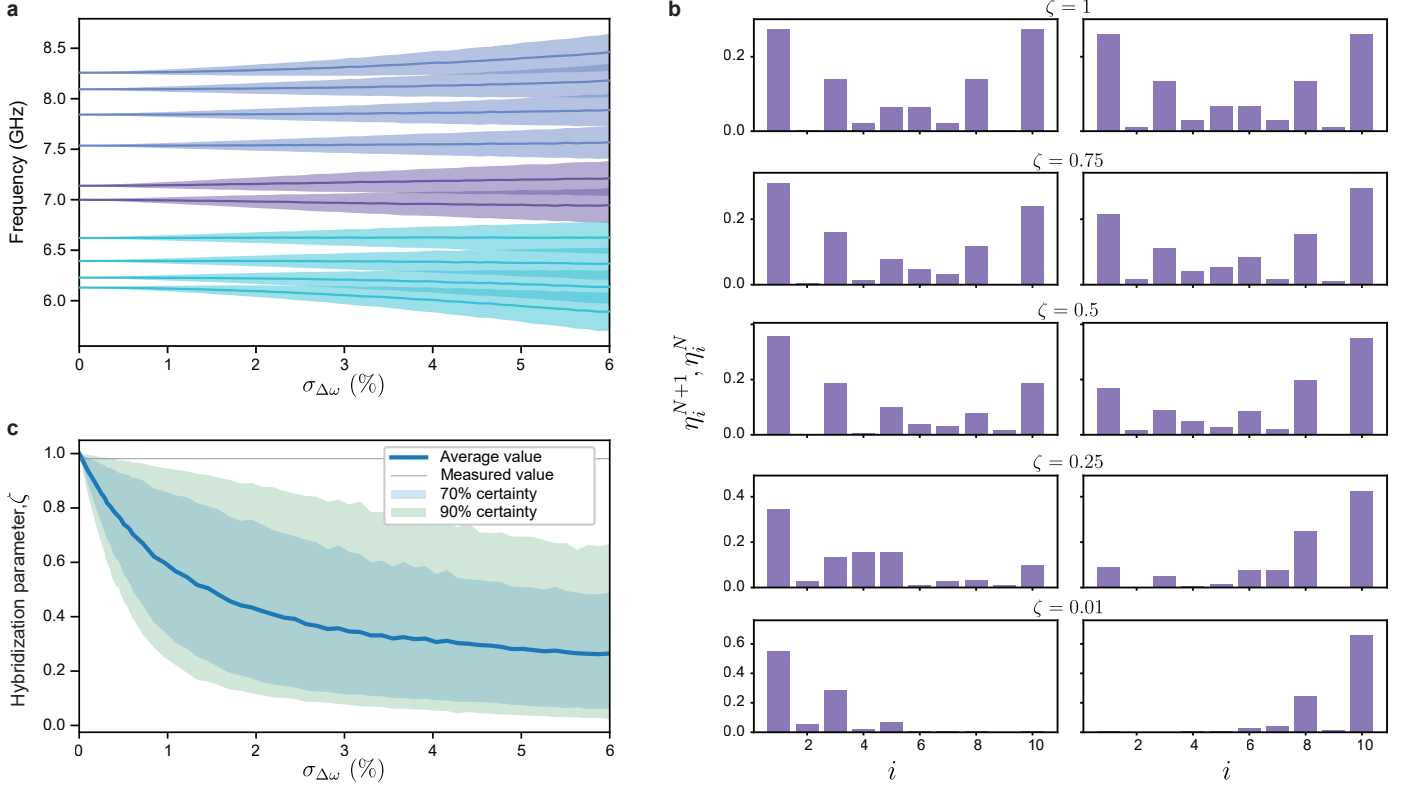


FIG. 2. **Disorder effect in SSH chains.** **a**, Effect of cavity frequency disorder on the mode spectrum of a 10 cell SSH chain considering the same parameters as the device discussed in the main text. For every relative frequency disorder standard deviation, $\sigma_{\Delta\omega}$, 4000 random cases were generated. The solid lines show the average mode frequency. The shades show the statistical standard deviation of mode frequencies. **b**, Example of disordered topological edge states with different hybridization factors, ζ . **c**, Plot of hybridization factor versus frequency disorder standard deviation. The solid blue line shows the statistical average over 4000 random points for each error percentage. The shades show bonds for 70% and 90% statistical certainty. The gray line identifies the measured hybridization factor in the 1D chain discussed in the main text.

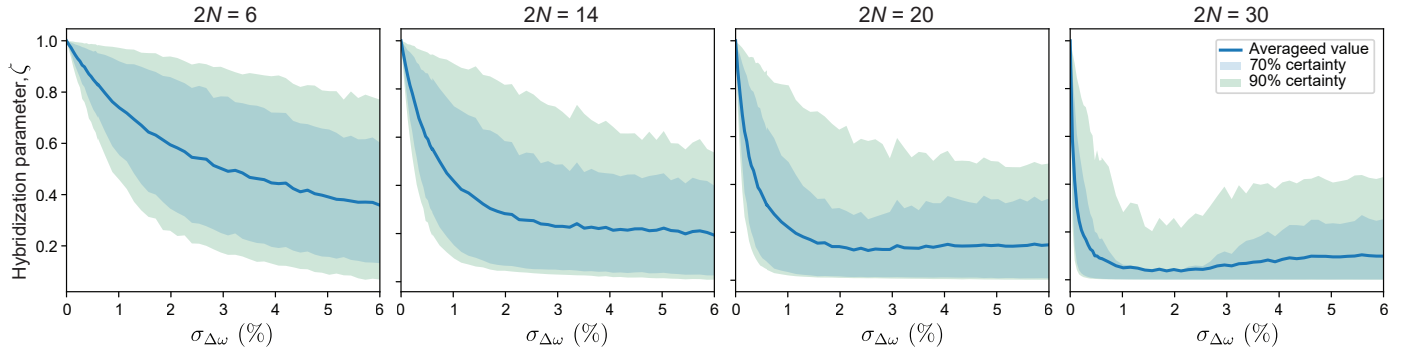


FIG. 3. **Disorder effect on hybridization for different chain lengths.** The hybridization factor ζ in relation to the frequency disorder is shown for several chain lengths with same the parameters. In longer chains, the hybridization is more sensitive to disorder.

in two edge states each one only localized on one end of the chain. To quantitatively describe this effect, we defined the edge states hybridization factor, ζ , defined by:

$$\zeta = \frac{1}{2} \left(\frac{\min(\eta_1^N, \eta_{2N}^N)}{\max(\eta_1^N, \eta_{2N}^N)} + \frac{\min(\eta_1^{N+1}, \eta_{2N}^{N+1})}{\max(\eta_1^{N+1}, \eta_{2N}^{N+1})} \right) \quad (42)$$

where η_i^N and η_i^{N+1} are the energy participation ratios of the topological edge modes in a $2N$ cell SSH chain. For a fully co-localized topological mode shape $\zeta = 1$, while it reduces to 0 for the fully non-hybridized (single side-localized) case (Fig. 2b). We calculated the average and standard deviation of ζ over the statistical pool for various $\sigma_{\Delta\omega}$. Figure 2c shows that hybridization is dramatically affected by disorder. Based on the mode shape measurement data presented in the main text, the hybridization factor for the 10 cell SSH device is $\zeta^{\text{meas}} = 0.98$ which corresponds to the stochastic frequency disorder in the range of $\sigma_{\Delta\omega} = (0.01\%, 0.38\%)$ with 90% certainty. This indicates small relative disorder in the gap size ($\sigma_{\Delta\text{gap}} = \frac{1}{2}\sigma_{\Delta\omega}$). It's worth mentioning that hybridization is also strongly affected by the length of the SSH chain, where for an example of 20 cell chain with the same parameters as the 10 cell case, the hybridization factor reduces sharply at smaller $\sigma_{\Delta\omega}$ as shown in figure 3.

B. SSH model with second nearest neighbor coupling and beyond

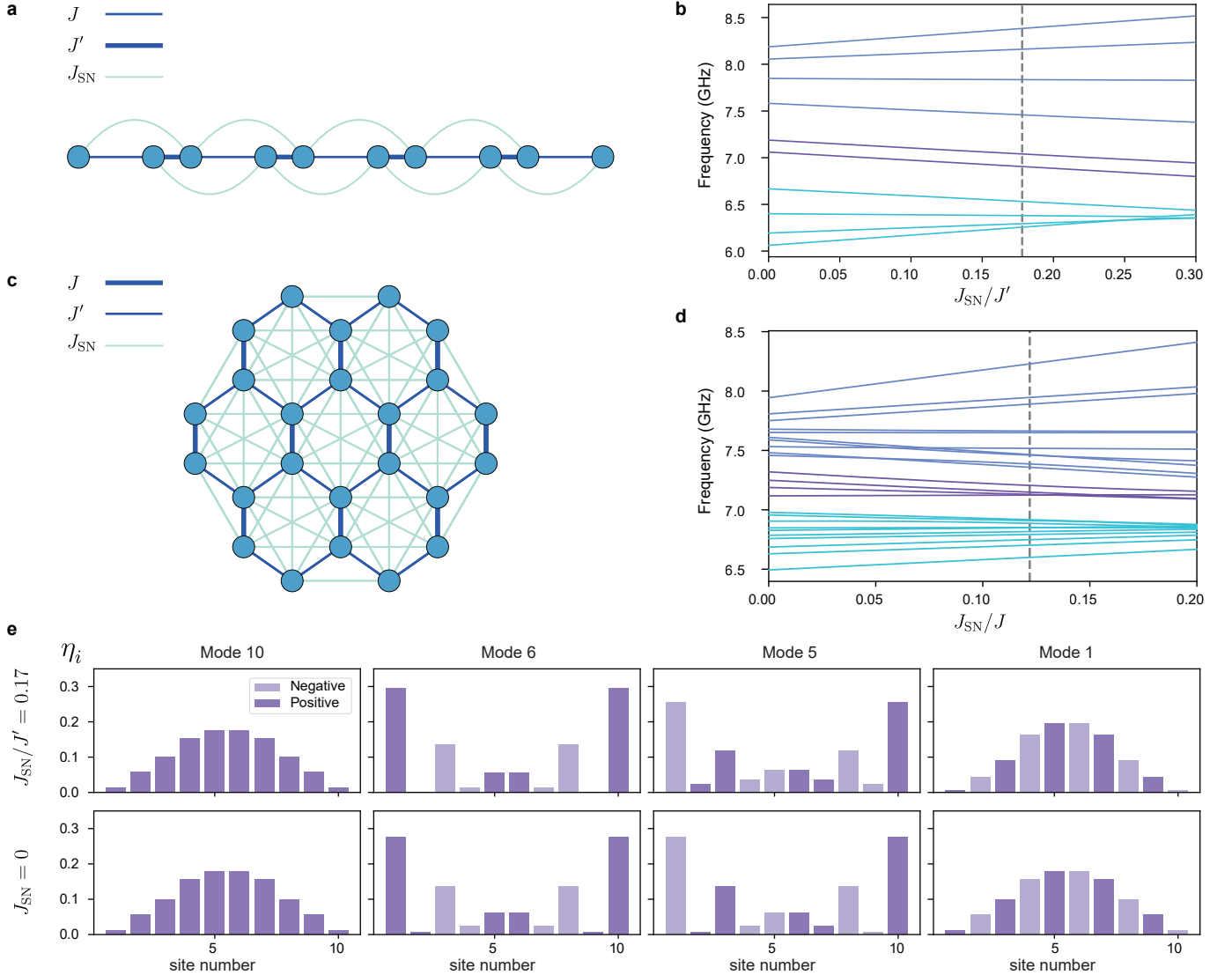


FIG. 4. **Second nearest neighbor coupling in SSH chains and lattices.** **a,b**, The mode diagram of a 1D SSH chain and 2D SSH-like honeycomb lattice respectively including second nearest neighbor couplings (SNNC). **b,d**, The energy spectrum of such lattices versus the relative SNNC strength for 1D and 2D cases respectively. The band structure will be asymmetric by introducing SNNC which breaks the chiral symmetry of the chain. the dashed line shows the SNNC values of the actual devices discussed in the main text. **e**, The comparison of the mode shapes between an ideal 10 site SSH chain and a chain with SNNC, showing a minor change in the mode shapes.

In most physical implementations of the SSH model in lattices, parasitic couplings between distanced sites are unavoidable and deviate the actual response of the devices from the ideal model. The effect of these higher-order couplings on the band structure, mode shapes, and topological properties of the SSH chains has been studied in several works [2–4]. Here we summarize these results and calculate the band structure of the designed devices in the presence of the parasitic coupling.

In our case, the higher-order couplings arise from the mutual inductance between distanced spiral inductors in LC circuits. The parasitic coupling rate decays with $J_{\text{par}} \propto \frac{1}{l^3}$, where l is the effective distance between two spirals. Figure 4 a,c shows the modified mode diagram including the second nearest neighbor (SNN) coupling J_{SN} . While the definition of SNN is clear in chains, in the honeycomb lattice, we extend this definition to all triangular sites with a shared edge since the mutual inductance between such triangles are approximately equal based on FEM simulations. Figures 4b,d shows the numerically calculated mode structure versus the relative SNN coupling rate for the 1D chain and the 2D honeycomb lattice discussed in the main text, respectively. As expected and analytically studied in cited references, the SNN coupling breaks the symmetry of the band structure resulting in a wider UPB and narrower LPB, while the edge states splitting and the band gap is barely affected.

The SNN coupling values extracted from the measurement is shown by a dashed line in figures 4b and 4c. When $J_{\text{SN}} < J/2$ in 1D chains the winding number remains one ($\mathcal{W} = 1$) indicating non-trivial topological properties and existence of edge states [3]. In our case $\frac{J_{\text{SN}}}{J'} = 0.17$ in the 1D chain device. Figure 4e shows the effect of SNN coupling on the mode shapes by comparing the ideal chain with the designed device.

C. Statistical analysis of orthogonality and measurement error

We discussed the optomechanical mode shape measurement technique in the main text to directly extract the eigenmodes (eigenvectors of the system Hamiltonian). In the theory section of the SI, we explained the iterative normalization method used to extract the mode shapes without the need to measure some hardly-accessible parameters of our system. To check the accuracy of our measurements and quantitatively verify the orthogonality of the mode shapes as eigenstates of the system, we show the inner product of every pair of modes, $|\sum_i \psi_i^* \psi_i^l|$ in figure 5a,b for 10 site 1D chain as well as 24 site honeycomb lattice. Since the measurement does not retrieve the phase in the mode shapes (i.e. positive or negative signs because such a system always results in real eigenvector and eigenvalues), we inferred the phases from the theoretical mode shape estimates. As it is shown in the figure, the 1D dataset manifests high orthogonality with a maximum $\sim 3\%$ inner product. The 2D dataset also shows small values except for a single mode (mode 17) which has a non-zero product with a few other modes. As a figure-of-merit, the average value of all inner products, $\frac{\sum_{k \neq l} \langle \psi^k | \psi^l \rangle}{2N \times (2N-1)}$, is 1.2% for the 1D chain and 5% for the 2D lattice.

To estimate the average error induced by the measurement process on the extracted eigenstates, we performed a simple numerical stochastic analysis. In a $2N$ -dimensional space, one can consider an ideal orthonormal set of vectors, $\{\mathbf{e}_k\}$, and add a $2N$ -dimensional Gaussian random variable with a standard deviation of σ to every element in order to create a disturbed set of $\{\mathbf{e}'_k\}$. Figure 5c shows the stochastic expected value and the 90% certainty range of the average inner product of the disturbed set, $\frac{\sum_{k \neq l} \mathbf{e}'_k \cdot \mathbf{e}'_l}{2N \times (2N-1)}$ for $2N = 10$ (1D) and $2N = 24$ (2D). Considering the measured average inner products, we conclude $\sigma \simeq 1\%$ for 1D and $\sigma \simeq 5\%$ for 2D devices.

Supplementary Note 4. Two dimensional honeycomb lattice

In this section, we discuss the bulk band structure as well as the topological phase transition of a honeycomb lattice. Hexagonal lattices are well studied in the context of quantum hall effect in graphene [5–9]. The hexagonal lattice is one of the simplest non-Bravais 2D lattices, which has two lattice points in one unit cell, enabling non-trivial topological properties.

In our work, a 2D optomechanical lattice is fabricated and characterized, as demonstration of the extendability of our system. We design the 2D lattice as a direct analog of the 1D SSH chain. Three unique directions exist in a hexagonal lattice, shown with different line styles in Fig. 6a. We only assign alternating coupling strength J and J' to intra-cell and inter-cell couplings, i.e. one direction is distinguished with the other two. Two lattice vectors are denoted as \mathbf{a}_1 and \mathbf{a}_2 in Fig. 6a. One unit cell, consisting of two lattice points, is enclosed in the green shaded area. The coordinate is chosen to have lattice vectors of unit length, i.e. $\mathbf{a}_{1,2} = (\pm \frac{1}{2}, \frac{\sqrt{3}}{2})$.

The Hamiltonian of such system can be formally written as:

$$\hat{H} = \sum_{\mathbf{i}-\mathbf{j}=\mathbf{a}_{1,2}} J' |\mathbf{i}, A\rangle \langle \mathbf{j}, B| + \sum_{\mathbf{i}} J |\mathbf{i}, A\rangle \langle \mathbf{i}, B| + \text{h.c.}, \quad (43)$$

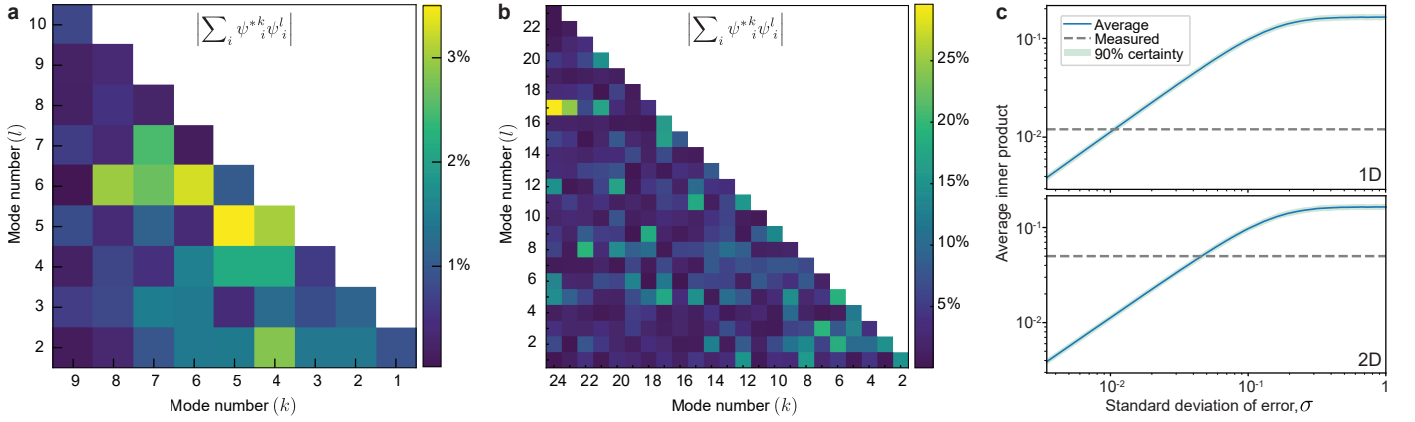


FIG. 5. **Inner products of the measured eigenstates as an indicator for measurement accuracy.** **a, b,** Scalar products between the measured mode functions after iterative normalization (introduced in the theory section) for 1D and 2D devices correspondingly. The inner products are a quantitative orthogonality verification of the measured mode shapes (eigenvectors) in those systems. **c** The stochastic analysis of the standard deviation of the equivalent Gaussian noise (σ) induced in the measurement on the eigenmodes. The expected value of the average inner products in a 10 (1D), and 24 (2D) dimensional space is shown versus σ . The grey lines indicate the measured average inner product.

where $|\mathbf{i}, A\rangle$ denotes an occupation at site $\mathbf{i} = m\mathbf{a}_1 + n\mathbf{a}_2$ and sublattice A .

A. Bulk Hamiltonian and Band Structure

Here we consider the Hamiltonian of an infinite honeycomb lattice (limit of $N \rightarrow \infty$), neglecting boundaries. The original Hamiltonian \hat{H} is written as the tensor product of a bulk Hamiltonian \hat{H}_{bulk} and an intra-cell Hamiltonian $\hat{H}(\mathbf{k})$ which is dependent on the wave vector \mathbf{k} , i.e. $\hat{H} = \hat{H}_{\text{bulk}} \otimes \hat{H}(\mathbf{k})$.

Given the translational symmetry of the lattice and Bloch's theorem, we expect plane wave form eigenstates of the bulk Hamiltonian. Thus, we introduce the plane wave basis as

$$|\mathbf{k}\rangle = \frac{1}{\sqrt{N}} \sum_{\mathbf{i}} e^{i\mathbf{i}\cdot\mathbf{k}} |\mathbf{i}\rangle, \quad (44)$$

where \mathbf{i} denotes a lattice point and \mathbf{k} takes value in the first Brillouin zone, shown with red in Fig.6b, together with the reciprocal lattice. The two reciprocal lattice vectors are $\mathbf{b}_{1,2} = (\pm 2\pi, \frac{2\sqrt{3}\pi}{3})$ in the coordinate we choose.

To obtain the intra-cell Hamiltonian $\hat{H}(\mathbf{k})$, we trace out the bulk degree of freedom and calculate $\langle \mathbf{k} | \hat{H} | \mathbf{k} \rangle = \langle \mathbf{k} | \hat{H}_{\text{bulk}} \otimes \hat{H}(\mathbf{k}) | \mathbf{k} \rangle = \hat{H}(\mathbf{k})$. Noting that

$$\langle \mathbf{i} | \hat{H} | \mathbf{i} \rangle = J(|A\rangle\langle B| + |B\rangle\langle A|), \quad (45)$$

$$\langle \mathbf{i} | \hat{H} | \mathbf{j} \rangle = J'(|A\rangle\langle B| + |B\rangle\langle A|), \quad (\mathbf{i} - \mathbf{j} = \mathbf{a}_{1,2}) \quad (46)$$

the reduced intra-cell Hamiltonian is obtained as

$$\begin{aligned} \hat{H}(\mathbf{k}) &= \langle \mathbf{k} | \hat{H} | \mathbf{k} \rangle = \frac{1}{N} \left(\sum_i e^{-i\mathbf{a}_i \cdot \mathbf{k}} \langle \mathbf{i} | \right) H \left(\sum_j e^{i\mathbf{a}_j \cdot \mathbf{k}} | \mathbf{j} \rangle \right) \\ &= \frac{1}{N} \left(\sum_i \langle \mathbf{i} | \hat{H} | \mathbf{i} \rangle + \sum_{i \text{ adjacent to } j} e^{i(\mathbf{j}-\mathbf{i}) \cdot \mathbf{k}} \langle \mathbf{i} | \hat{H} | \mathbf{j} \rangle \right) \\ &= |A\rangle\langle B| (J + J' (e^{i\mathbf{a}_1 \cdot \mathbf{k}} + e^{i\mathbf{a}_2 \cdot \mathbf{k}})) + h.c. \\ &= \begin{pmatrix} 0 & J + J' (e^{i\mathbf{a}_1 \cdot \mathbf{k}} + e^{i\mathbf{a}_2 \cdot \mathbf{k}}) \\ J + J' (e^{-i\mathbf{a}_1 \cdot \mathbf{k}} + e^{-i\mathbf{a}_2 \cdot \mathbf{k}}) & 0 \end{pmatrix}. \end{aligned} \quad (47)$$

This two level system Hamiltonian could also be written in terms of Pauli matrices, i.e. $\hat{H}(\mathbf{k}) = \boldsymbol{\sigma}(\mathbf{k}) \cdot (\hat{\sigma}_x, \hat{\sigma}_x, \hat{\sigma}_z)$, where

$$\boldsymbol{\sigma}(\mathbf{k}) = (J + J' \text{Re}(e^{-i\mathbf{a}_1 \cdot \mathbf{k}} + e^{-i\mathbf{a}_2 \cdot \mathbf{k}}), J' \text{Im}(e^{-i\mathbf{a}_1 \cdot \mathbf{k}} + e^{-i\mathbf{a}_2 \cdot \mathbf{k}}), 0). \quad (48)$$

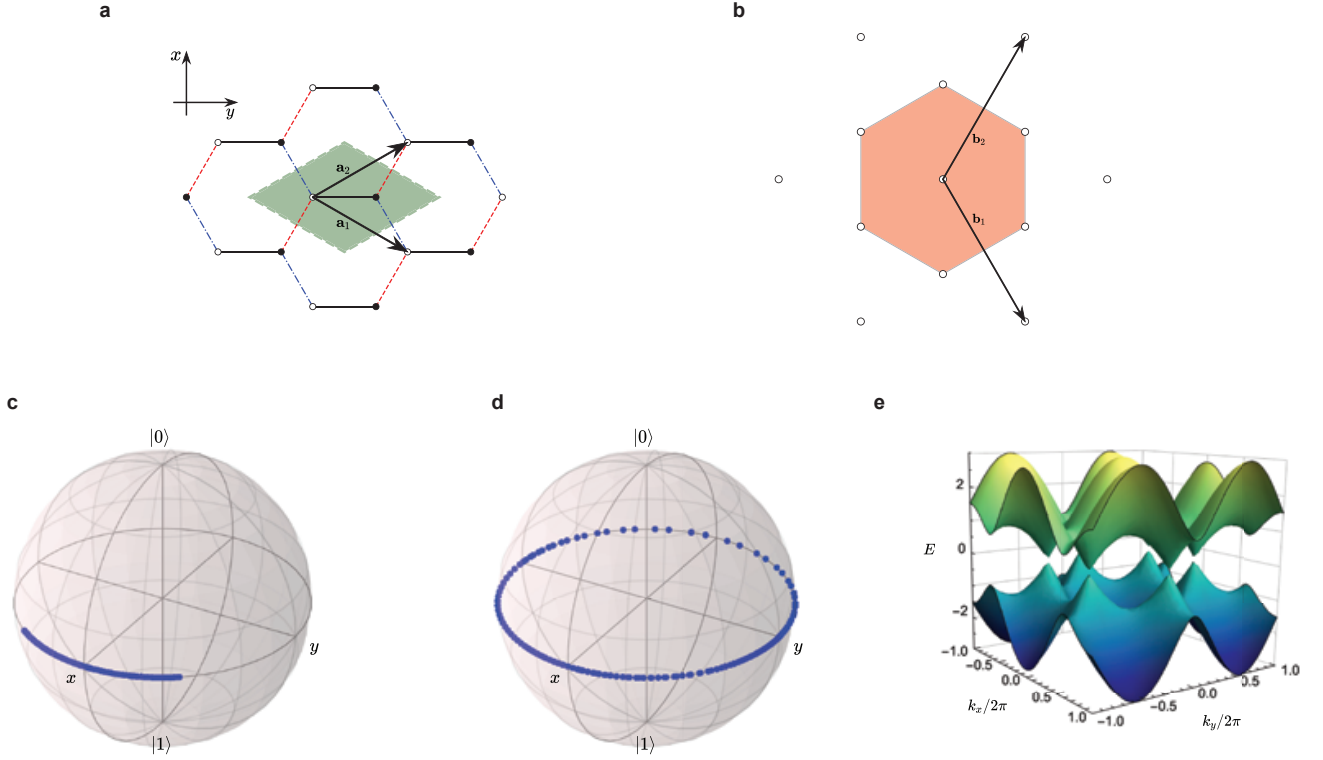


FIG. 6. **Two dimensional honeycomb lattice theory.** **a** Direct hexagonal lattice: the unit cell and lattice vectors are shown. **b** Reciprocal hexagonal lattice: the first Brillouin zone is shown. **c** Trace of $\sigma(\mathbf{k})$ for $J/J' = 0.3$. **d** Trace of $\sigma(\mathbf{k})$ for $J/J' = 0.7$. **e** Band structure for $J/J' = 1$.

The band structure could be obtained from diagonalizing the intra-cell Hamiltonian as

$$E(\mathbf{k}) = \pm \left| \begin{pmatrix} J + J' \cos(\mathbf{k} \cdot \mathbf{a}_1) + J' \cos(\mathbf{k} \cdot \mathbf{a}_2) \\ J' \sin(\mathbf{k} \cdot \mathbf{a}_1) + J' \sin(\mathbf{k} \cdot \mathbf{a}_2) \\ 0 \end{pmatrix} \right|. \quad (49)$$

Two bands are shown in Fig. 6e, contacting each other at the corners of Brillouin zone, i.e. the Dirac points. Chiral symmetry is still retained in the honeycomb lattice, thus the two bands have opposite energies.

B. Representation on the Bloch Sphere

As discussed in the last section, the diagonal elements are zero for a honeycomb lattice, similar to the 1D SSH model. Thus, the adiabatic trace of $\sigma(\mathbf{k})$ is still restricted to the equator of the Bloch sphere. Figures 6c,d shows the numerical calculations of the normalized $\sigma(\mathbf{k})$ on the Bloch sphere as \mathbf{k} traverses the first Brillouin zone, for $J'/J = 0.3$ and $J'/J = 0.7$ respectively. This manifests a similar behavior as in the 1D SSH model. For different J'/J , $\sigma(\mathbf{k})$ either winds around the full equator of the Bloch sphere (*topological* phase), or stays as an open loop within half of the Bloch sphere (*trivial* phase).

C. Topological phase transition

The phase transition threshold between trivial and topological phases differs from the 1D case, where it happens at $J/J' = 1$. As \mathbf{k} evaluated in the Brillouin zone, the vector $\sigma(\mathbf{k})$ takes value in the $x - y$ plane. The phase transition happens when the range of $\sigma(\mathbf{k})$ includes the origin of the $x - y$ plane.

A point $(\mathbf{k}_x, \mathbf{k}_y)$ is mapped to

$$\sigma(\mathbf{k}) = (J + 2J' \cos(\sqrt{3}\mathbf{k}_y/2) \cos(\mathbf{k}_x/2), 2J' \sin(\sqrt{3}\mathbf{k}_y/2) \cos(\mathbf{k}_x/2), 0). \quad (50)$$

As $(\mathbf{k}_x, \mathbf{k}_y)$ traverse the Brillouin zone, $\sigma(\mathbf{k})$ covers a circle, which is centered at $(J, 0)$ and has a radius of $J'/2$. Then the phase transition point is determined as $J'/J = 2$, when the circle intersects the origin.

D. Design of the 24 site honeycomb lattice

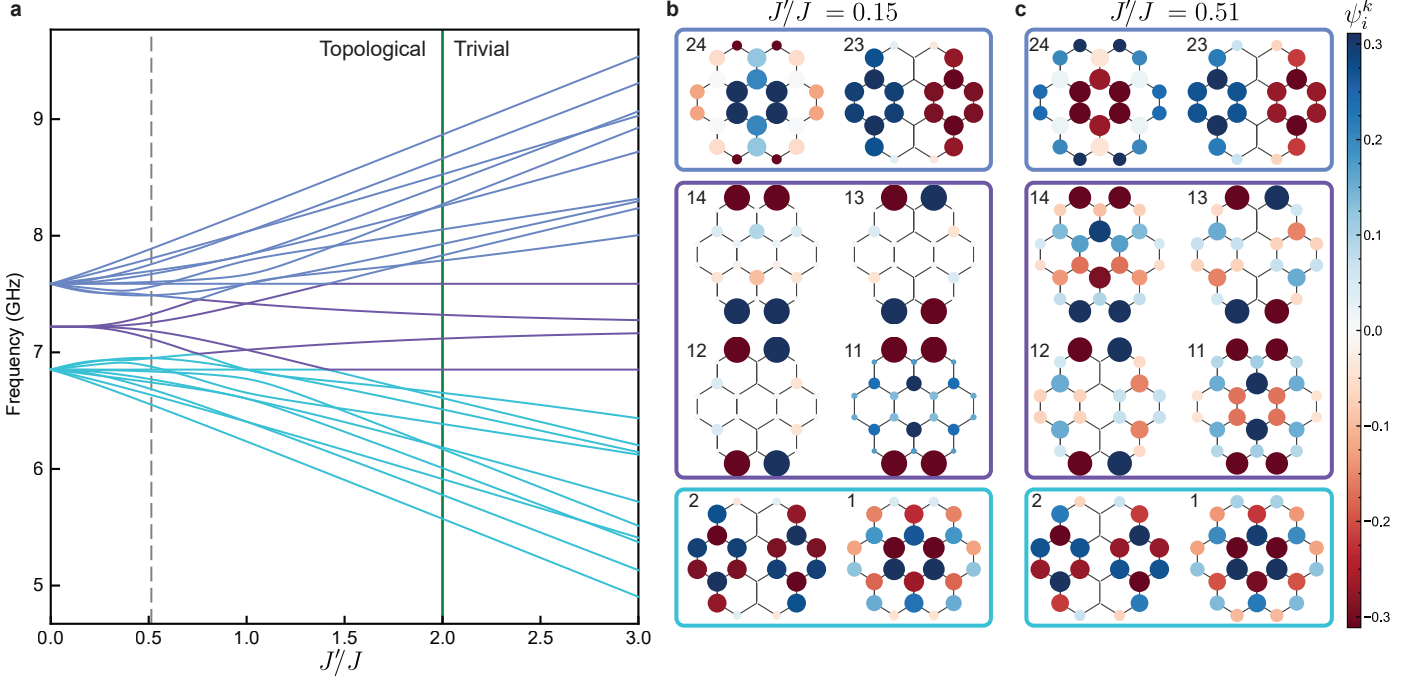


FIG. 7. **24 site honeycomb lattice design.** **a**, Mode structure of the 24 site honeycomb lattice introduced in the main text versus J'/J . The green line shows the topological phase transition and the dashed gray line shows the design parameter. **b,c**, Examples of the mode shapes in UPB, topological states, and LPB for $J'/J = 0.15$ and $J'/J = 0.51$ (design values) respectively.

After the discussion on the band structure of the infinite 2D honeycomb lattice and finding out the phase transition condition, we consider a 24 site lattice introduced in the main text. To design the system parameters (J and J') we calculate band structure for the 24 site system while sweeping J'/J as shown in figure 7a. In the topological phase, 4 edge states are separated from UPB and LPB. Figure 7b,c shows an example of mode shapes for $J'/J = 0.15$ and $J'/J = 0.51$ (design target) in UPB, LPB, as well as four edge states showing high energy participation on edge sites with different symmetries.

Supplementary Note 5. Design and simulation

A. Design principles

Here we review design rules and relations between the system parameters and the geometrical parameters of the circuits. First we consider a single building block microwave LC resonator. The capacitance of a vacuum-gap capacitor can be approximated by $C_{VG} = \frac{\epsilon_0 A_{\text{eff}}}{d}$, where A_{eff} is the effective area of the parallel plate and d is the gap size. The self-inductance or mutual inductance of a spiral inductors can be precisely calculated using Neumann's formula:

$$L_{A,B} = \frac{\mu_0}{4\pi} \oint_A \oint_B \frac{d\mathbf{r}_A \cdot d\mathbf{r}_B}{|\mathbf{r}_A - \mathbf{r}_B|} \quad (51)$$

Where the path integral is carried out over the geometrical curve of the spiral. In the case of self inductance $A = B$ and in case of mutual inductance A and B refer to the shape functions of the two spirals. This results in two simple approximate scaling rules: The self inductance of a spiral scales with $L \propto N_s^2 r_{\text{eff}}$ where N_s is the number of

turns and r_{eff} is the effective radius of spiral. The mutual inductance between two spirals A and B with the distance of l scales with $M \propto N_{s,A} N_{s,B} r_{\text{eff},A}^2 r_{\text{eff},B}^2 / l^3$ in far distances ($l \gg r_{\text{eff},A}, r_{\text{eff},B}$). To increase microwave coupling rates ($J = \omega_c \frac{M}{2L}$) in a design, M needs to increase while L is fixed. This can be achieved by increasing the aspect ratio of spirals to have longer adjacent wires in neighbor sites, like the spirals used in the 10 site 1D chain.

The mechanical frequency of the first fundamental mode of a drumhead resonator can be approximated as $\Omega_m \simeq \frac{2.4}{R} \sqrt{\frac{\sigma^{Al}}{\rho^{Al}}}$ where R is the radius of the drumhead (radius of the circular trench as fixed mechanical boundary condition) and σ^{Al} , ρ^{Al} are the stress and the density of the Al thin film. In the device, we slightly change the trench radius of different sites to distinguish them in further experiments. We note that this slight variation on the trench radius does not have a significant effect on the electrical boundary conditions of the circuit, and does not perturb the microwave resonance frequencies of LC circuits, ω_c .

To probe the system, the two ends of the chain are inductively coupled to coplanar waveguides using two short-circuited inductive loop couplers. The external coupling rate to the outermost sites is designed to be comparably smaller than internal microwave couplings in the chain to avoid deviation from the ideal SSH model (See Fig. 9).

B. Electromagnetic simulations

All the electromagnetic simulations were performed using Sonnet®. We first simulated the single LC resonator and varied the geometric inductor parameters and bottom capacitor plate diameter (which changes the capacitance) to get the desired resonance frequency around 7 GHz. As detailed in Sec. 2, when two harmonic modes get coupled together, two hybridized modes appear (Fig. 8 a inset). The frequency splitting between such two modes is exactly

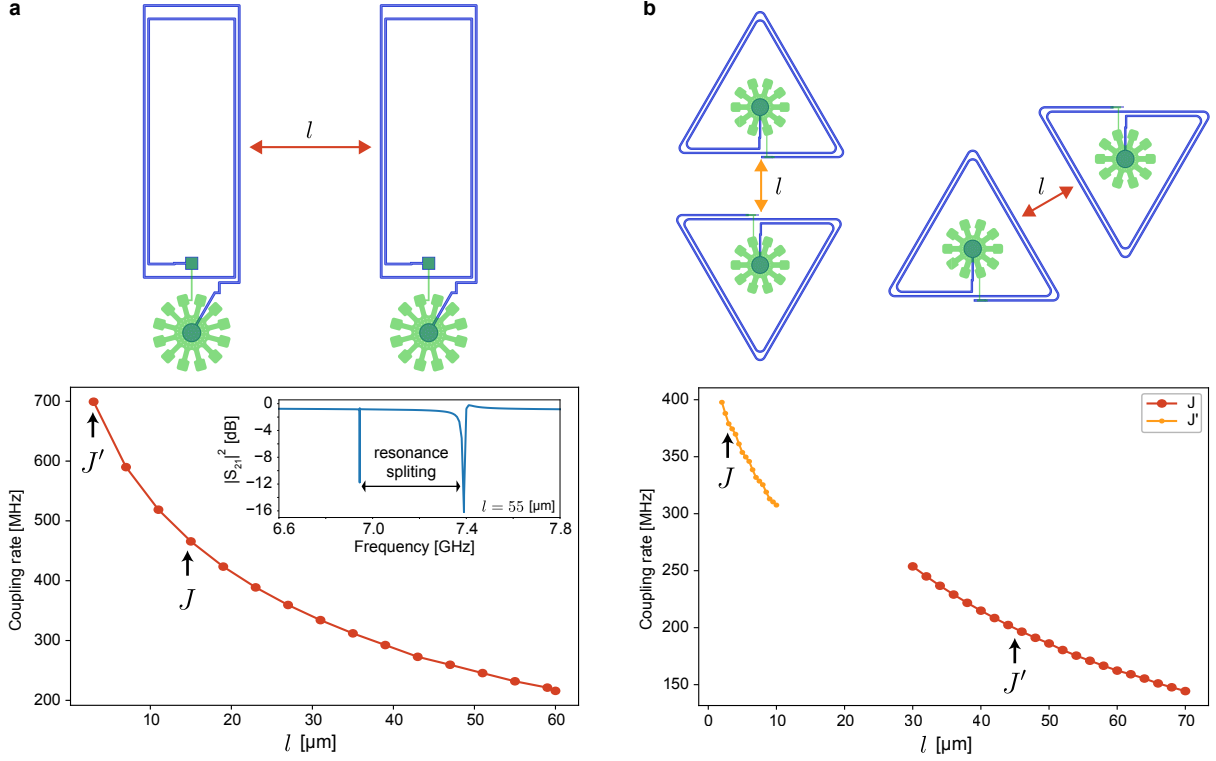


FIG. 8. Mutual coupling rate as a function of the distance between two identical sites **a**, 1D unit cell. **(b)**, 2D unit cell.

double the coupling rate between them as can be easily seen from Eq. (35). In our case, the coupling rate between two neighbouring modes is inductive, and its strength can be changed by varying the distance between them. We ran parametrised Sonnet® simulations by varying the distance between them, and for each run we extracted the coupling rate from the resulting frequency splitting. As the distance between the two circuits increases, the coupling rate decreases, as it is expected. (See Fig. 8)

From these simulations we choose the distances that would result in the coupling strengths that we desired. For

the 1D case (Fig. 8 a) there is one direction of coupling. In the graph the chosen values of the inter-cell coupling J' and intra-cell coupling J can be seen. From these same simulations unwanted second and third order coupling rates can also be extracted, which we used to compute the expected mode shapes. For the 2D case (Fig. 8 b) we ran two different distance sweeps because of the slightly asymmetric shape of the spiral inductor, due to the needed crossover point to connect it to the capacitor plates.

Another important aspect is how much the input/output loop couplers are shifting the resonance frequency of the outermost sites. If the loop coupler is too close to the circuit, we get a resonance frequency shift, which will only affect the edges of the array, seriously impairing the hybridization of the modes. To study this effect, after having optimized the dimensions of the loop itself, we swept the distance to a single LC site. In Fig. 9 the external coupling rate - resonance shift tradeoff is shown. We chose a distance that could provide a sufficiently high coupling rate, but

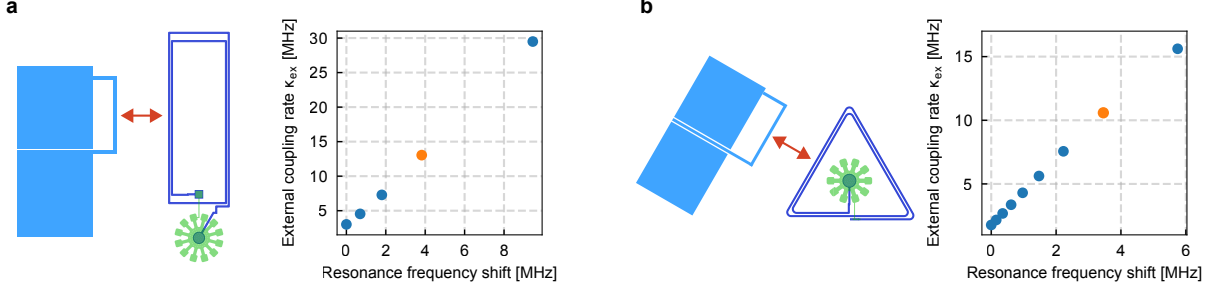


FIG. 9. **Coupling to the input-output waveguide as a function of distance.** Sweeping the distance of a single site to the loop coupler for the 1D (a) and 2D (b) design, the external coupling rates as well as the resonance frequency shift due to probing the system are extracted. The orange dot corresponds to the distance chosen in the final designs.

for which the resonance frequency shift was much lower than the coupling rates in the system $\Delta\omega_c/2\pi \ll J, J'/$.

Finally, the whole device can be simulated in Sonnet®. The result can be seen in Fig. 10. For the 1D we directly simulated the mask designed used in the fabrication process. For the 2D, given the size of the structure, we substituted the vacuum-gap capacitors with ideal capacitor components. This should not change the coupling between the sites in an appreciable way because the electromagnetic field of the vacuum-gap capacitor is confined between the plates, and the magnetic field responsible for the coupling of neighbouring sites is mostly confined around the spiral lines.

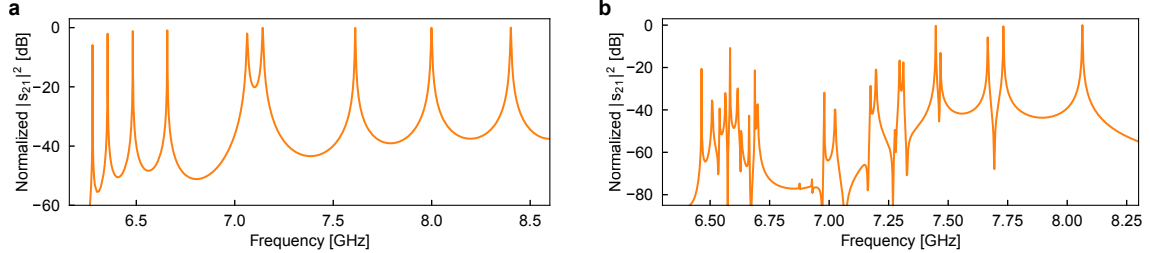


FIG. 10. **Sonnet® simulation of the full designs.** (a), 1D array. (b), 2D lattice.

Supplementary Note 6. Nanofabrication techniques

A. Challenges and limitations of the conventional fabrication process

Since 2010, when the conventional nanofabrication process of making superconducting vacuum-gap capacitors was introduced by Cicak *et al.* [10] the design and process did not have substantial change, while it was used to implement outstanding quantum experiments in optomechanics. The main steps of the conventional process (Fig. 11a) consist of deposition and definition the bottom plate of the capacitor, deposition of a sacrificial layer covering the bottom layer, deposition and definition of the top capacitor plate, and finally releasing the device by removing (isotropic etching) the sacrificial layer. Following the same principle, several research groups realized circuit optomechanical systems using various set of sacrificial materials on different substrates such as Si_3N_4 on sapphire at NIST [11], polymer on Si at Caltech [12], SiO_2 on quartz at Aalto [13], and aSi on sapphire at EPFL [14]. Due to the deposition induced

compressive stress in the superconducting thin film (mostly Al), the drumhead capacitor is buckling up after the release, which increases the gap size up to a few micro meters. Cooling down such devices, induces tensile stress in the Al film due to the high thermal expansion rate difference with the substrate. Under the tensile stress, the drumhead shrinks and buckles in the opposite direction, resulting in a small, but not accurately predictable, nor reproducible, gap size in the order of ~ 50 nm. This prevents precisely controlling microwave and mechanical properties of the system at low temperatures and reduces reproducibility of the design given the high probability of deformations and collapses after the release [15].

B. The new reproducible nanofabrication process for circuit optomechanics

Here we present a novel nanofabrication process (Fig. 12) to overcome such challenges with a significant improvement on control and yield. We define a trench in the substrate containing the bottom plate of the capacitor. The trench then gets covered by a thick SiO_2 sacrificial layer, which inherits the same topography of the layer underneath. To remove this topography and obtain a flat surface, we use chemical mechanical polishing (CMP) to planarize the SiO_2 surface. We then etch back the sacrificial layer down to the substrate layer and deposit the top Al plate of the capacitor. Although after the release of structure by HF vapor etching of SiO_2 the drumhead will buckle up due to the compressive stress, at cryogenic temperatures the high tensile stress ensures the flatness of the top plate. This will guarantee the gap size to be precisely defined by the depth of the trench and the thickness of the bottom plate. We describe every step of the process in detail here: We use high-resistivity silicon wafers (Fig. 12a). First,

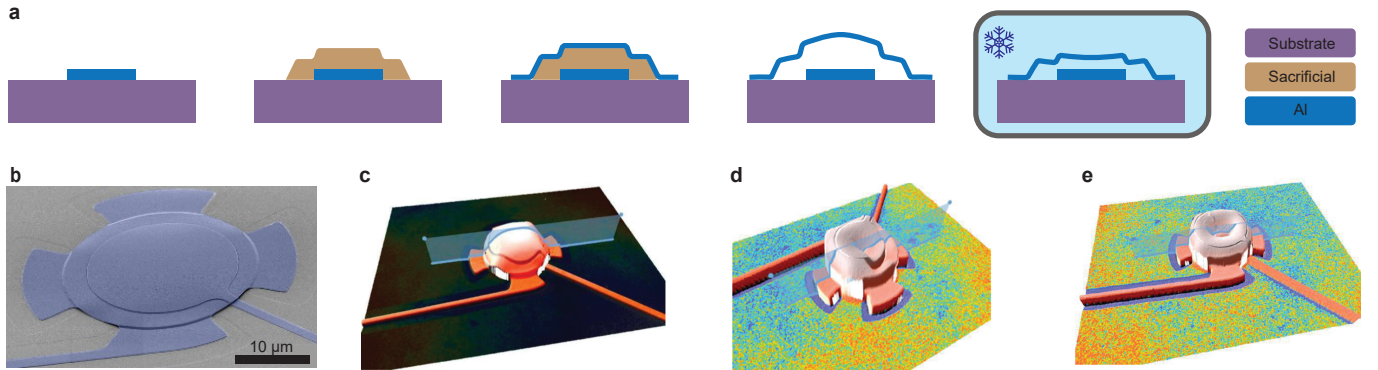


FIG. 11. Challenges of the conventional fabrication process for electromechanics. **a**, The traditional nanofabrication process used to make mechanically compliant vacuum-gap capacitors: a sacrificial layer (aSi or Si_3N_4) used to support the top layer. After the release, the capacitor buckles up more than $1 \mu\text{m}$ due to the compressive stress in deposited superconducting metal. At low temperatures, the drumhead shrinks resulting in a small gap size of ~ 50 nm. **b**, SEM image of a drumhead fabricated with the conventional process at EPFL[16]. **c**, Laser profilometry of a successfully released drumhead. **d,e**, Laser profilometry of a deformed and a collapsed drumhead correspondingly.

a 325 nm trench is etched in the silicon substrate to define the bottom part of the circuit (Fig. 12b). Silicon etching is done by deep reactive ion etching (DRIE) with C_4F_8 gas (Adixen AMS200). The next step is the deposition of 100 nm aluminum by electron beam evaporation (Alliance-Concept EVA 760, Fig. 12c). We pattern and etch Al using wet etchant (H_3PO_4 85% + CH_3COOH 100% + HNO_3 70% 83:5.5:5.5, Fig. 12d). Afterwards, we deposit 2 μm silicon oxide using low thermal oxide deposition (LTO) (Fig. 12d). To remove the surface topography, we use CMP (ALPSITEC MECAPOL E 460) to planarize the surface (Fig. 12f) and reduce the surface topography to less than 10 nm (an example of the polishing process is shown in Fig. 13). We made dummy trenches on all the empty space of the wafer to increase the uniformity in the CMP process. After planarization we etch back the sacrificial layer by ion beam etcher (IBE, Veeco Nexus IBE350) to land on the silicon substrate (Fig. 12g). Before deposition of the top plate Al, we make an opening in the oxide to ensure the galvanic connection between top and bottom layers of the circuit in the spiral inductor and capacitor. This is done by DRIE etching of the SiO_2 (SPTS APS) with CHF_3 . Prior to the opening etch, the photo-resist is re-flowed to make slanted sidewalls to smoothly connect two layers. Then we use a 1:1 DRIE etch of SiO_2 (SPTS APS with CHF_3 etchant), where the resist pattern is transferred to the oxide (Fig. 14b). The top Al layer (200 nm) is evaporated afterwards to form the top plate of the vacuum-gap capacitor. After dicing the wafer into chips, we finally release the structure using Hydrofluoric (HF) acid vapor (SPTS uEtch) which is an isotropic etch process dedicated for MEMS structuring and does not attack Al. The holes on the drumhead are there to facilitate the release process. All patterning steps are done by direct mask-less optical lithography (Heidelberg

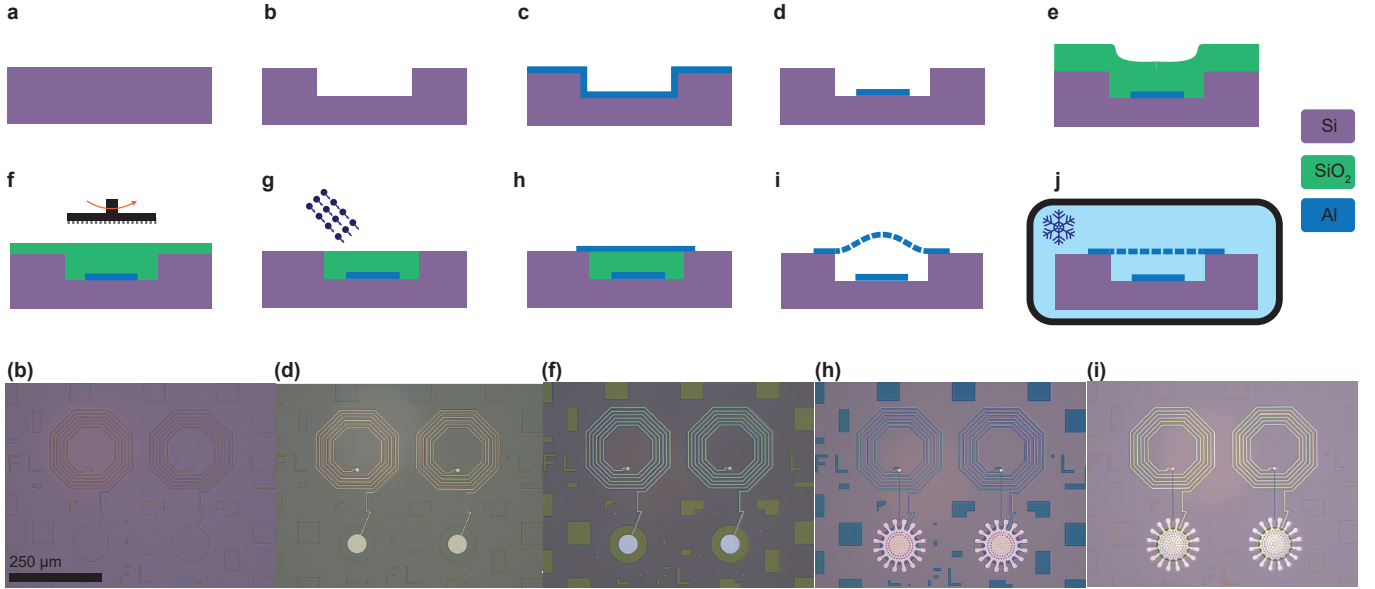


FIG. 12. The new reproducible nanofabrication process for circuit optomechanics. **a, b**, Etching a trench in a silicon wafer (325 nm). **c**, Aluminum deposition of the bottom plate (100 nm). **d**, Patterning of Al. **e**, SiO₂ sacrificial layer deposition (3 μ m). **f**, CMP planarization. **g**, landing on the substrate using IBE etching. **h**, Top Al layer deposition and patterning (200 nm). **i**, Releasing the structure using HF vapor. Due to compressive stresses, the top plate will buckle up. **j**, At cryogenic temperatures, the drumhead shrinks and flattens. The optical micrographs shows selected steps of the process flow

MLA 150) using 1 μ m photo resist (AZ ECI 3007).

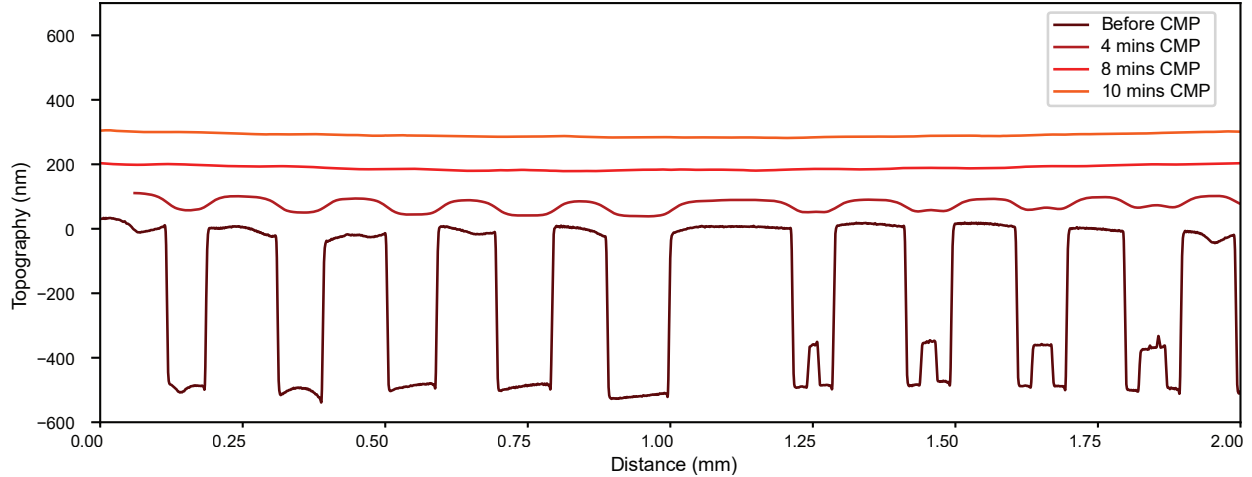


FIG. 13. Chemical mechanical polishing (CMP) for removing the surface topography. CMP enables us to reduce the surface topography from ~ 500 nm to below 10 nm. The figure shows the effect of sequential CMP steps on the topography measured by mechanical profilometry. The final global curve is the wafer bow.

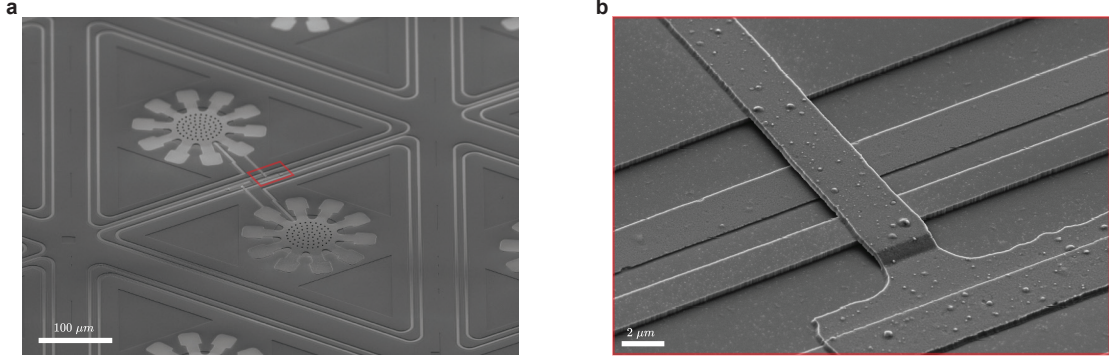


FIG. 14. **Honeycomb lattice.** **a**, SEM micrograph of the triangular building blocks of the honeycomb lattice. **b**, The galvanic connection of top and bottom Al layers and the crossovers of the spiral inductor.

Supplementary Note 7. Experimental setup and measurement techniques

A. Full experimental setup

The full experimental setup (Fig.15a) consists of a room-temperature (RT) and a cryogenic section. At RT, two Rohde & Schwartz (R&S) SMB 100A analog microwave sources generate the cooling/probe and excitation pumps, a R&S ZNB20 Vector Network Analyzer (VNA) and a R&S FSW 26 Electronic Spectrum Analyser (ESA) are used for the measurement itself. The VNA measures the coherent response of the devices, in our case the transmission

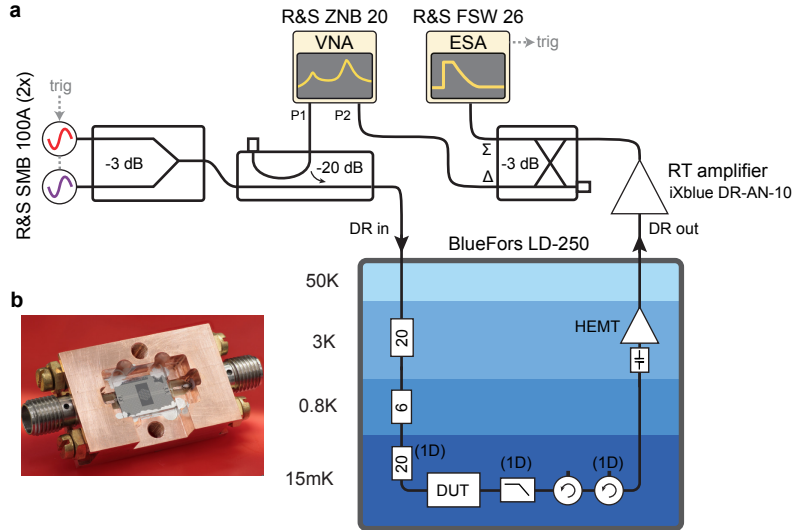


FIG. 15. **Full experimental setup used for the chips' characterization.** Some elements of the input line (inside round brackets) are specific only to the 1D sample. **b**, Packaged chip inside the copper sample holder.

scattering parameter $S_{21}(\omega)$. The ESA is not used in its usual frequency-domain mode, instead, for our experiment we use it in the so-called 'zero-span'. In this mode the instrument demodulates at a fixed CW frequency and effectively implements a time-domain power measurement over a large dynamic range, which is typical of spectrum analysers. The ESA is able to trigger the microwave sources to start the time-domain sequence, which is programmed in the sources. All the instruments are locked together and to a SRS FS725 Rubidium Frequency Standard to achieve frequency stability and accuracy. The two microwave sources are combined at RT through a 3dB microstrip coupler. The VNA is then directionally-coupled with 20dB of insertion loss and all the signals are finally sent to the Dilution Refrigerator (DR).

A series of cryogenic attenuators are used at the different flanges to thermally anchor the input wiring and more importantly to remove the room temperature noise from the input signal. For the 1D sample a total of 46 dB of nominal attenuation were used. For the 2D samples a total of 26 dB of nominal attenuation were used. In this

experiment we are not interested to probe the devices at the single photon level, hence the not-so-high attenuation values. We are more interested in being able to reach the regime where the effective mechanical damping rate greatly exceeds the intrinsic one $\Gamma_{\text{eff}} \gg \Gamma_m$ through optomechanical sideband cooling, which requires high on-chip powers. For the 1D chip an additional K&F 18GHz lowpass filter and circulator were used.

The output signal from the chips is firstly amplified with a cryogenic High Electron Mobility Transistor (HEMT) amplifier at the 4K flange of the DR. The HEMTs were both from Low-Noise-Factory, model numbers are LNF-LNC4.8C and LNF-LNC1.12A for the 1D and 2D sample respectively. The typical gain is 40 dB. The circulators placed after the chips are crucial in preventing the back-propagating high-amplitude signals of the HEMT amplifier from reaching the chip. A room temperature amplifier, model number iXblue DR-AN-10 is placed as close to the fridge as possible to further amplify the signal and make it robust against injected noise along the cables until they reach the measurement equipment. This signal is then split with a 180-hybrid coupler and sent back to port 2 of the VNA and the ESA.

The chip holder (Fig. 15b) is mounted at the MXC flange of the DR, which has a temperature of $T \approx 15$ mK. The chip holder is constructed with Oxygen-free copper. The CPW signal lines are wire bonded, as well as the ground plane close to them, while the perimeter ground plane has been contacted using conductive silver glue.

B. Ringdown data analysis and cavity shifts

The core of the mode shape measurement is the extraction of the energy participation ratio η_i^k of site i to collective microwave mode k by fitting the mechanical oscillator damping rate trend $\Gamma_{\text{eff},i}$ at site i with changing power. We extract the effective mechanical damping rates by measuring how fast each mechanical oscillator rings down from a high-photon occupancy state. This is the so-called ringdown measurement. We fit the ringdown data, an example data set of which can be seen in Fig. 16a, with an exponential profile $P(t) = P_0 \exp(-\Gamma_{\text{eff}}/2\pi) + N$ and extract Γ_{eff} from such fit. Given the very large amount of ringdown traces ($\# \text{ powers} \times (\# \text{ sites}) \times (\# \text{ collective modes}) = (5'100$

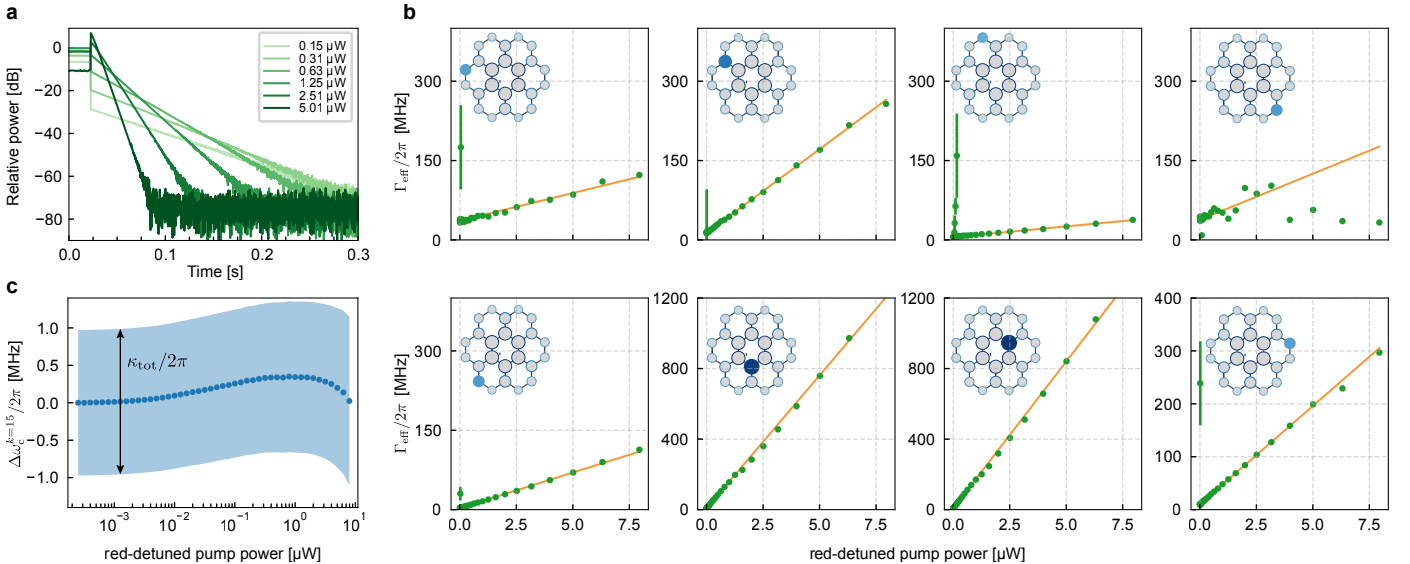


FIG. 16. **Data analysis.** **a**, Example raw data set of ringdowns with increasing cooling power. **b**, Γ_{eff} vs cooling power data for some sites of the $k = 24$ collective mode of the 2D sample. **c**, Collective mode resonance frequency shift versus cooling power for the average-linewidth mode with $\kappa/2\pi = 2$ MHz. The shaded area indicates the mode's linewidth.

for the 1D and 29'236 for the 2D sample), a robust automated fitting algorithm has been advised to reliably find good initial parameters for the fits. Another challenge arises because, due to the large variation of η_i^k across the different modes and sites, there can be more than 2 orders of magnitude in the exponential decay rate of the measured signal, as can be seen in Fig. 16b. This makes it difficult to have a one-for-all starting condition for the fits. Moreover, the initial decay of a highly-excited mechanical oscillator can exhibit non-linear behaviour due to the high-amplitude oscillations and it should not be included in the exponential fit. Finally, since for the optomechanical damping effect the relative detuning between the cavity and mechanical frequency is relevant, we measured the collective modes' resonance frequency shift with the cooling powers used for the experiment. Figure 16c shows an example of such analysis for mode $k = 15$ which has a linewidth closest the average among all the modes. We can see that for this

mode the cavity shift is negligible compared to the linewidth. This might not be the case for the modes with the lowest linewidths, and it could justify restricting the fitting to a lower-power range. This effect can also be taken into account by plugging in the correct $\tilde{\omega}_c^k$ and κ_{tot}^k into the optomechanical damping rate equation (19).

C. Mode shape extraction methods comparison

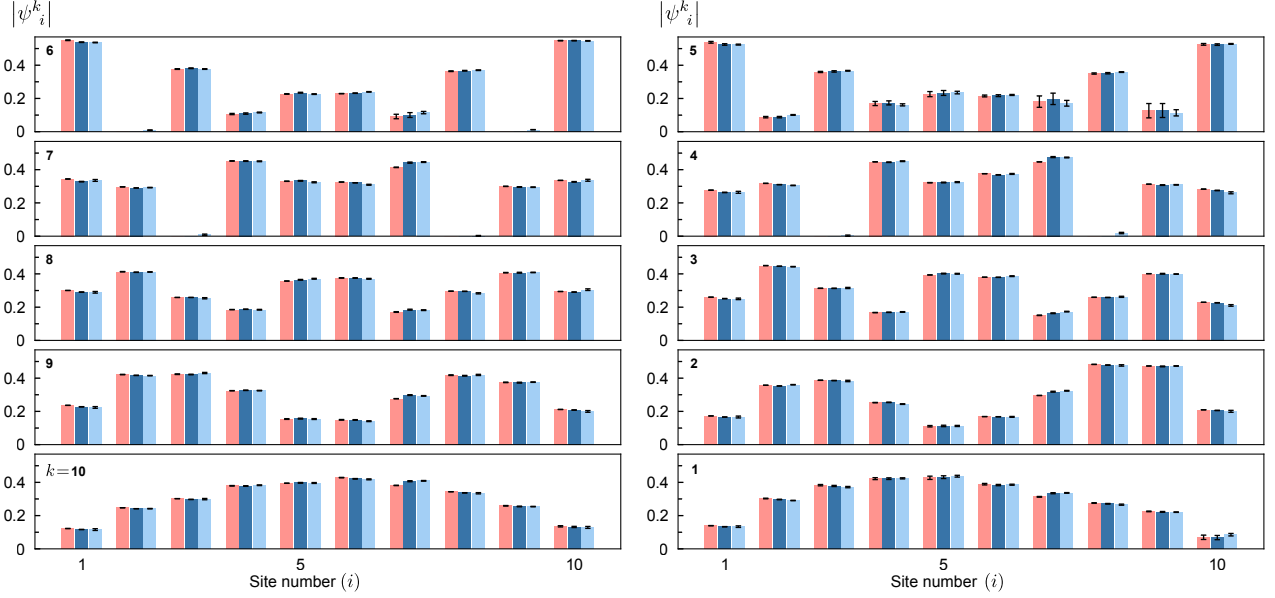


FIG. 17. **Three different mode shape extraction methods comparison.** The red bars are with the single-step normalization for each collective mode. The dark blue bars are with the iterative normalization method (presented in the main text). The light blue bars are mode shapes corrected based on the orthogonalization property of the unitary matrix.

As explained in section 1B, to extract the mode shapes we have to go through at least one normalization step.

$$\widetilde{\eta_i^k} \rightarrow \frac{\widetilde{\eta_i^k}}{\sum_i \widetilde{\eta_i^k}} \quad \forall k$$

This step is very intuitive as we are summing over all sites (i) in a given collective mode (k): the total input power gets distributed along the sites according to their participation ratio η_i^k , and all the participation ratios in a given collective mode must sum up to 1.

Next, we make use of the normalization conditions of the unitary matrix, and perform the iterative normalization process described in section 1B. These are the mode shapes presented in Figs. 3 and 4 of the main text.

As described Sec. 1C, in order to accurately reconstruct the Hamiltonian shown in Fig. 3 of the main text, the mode shapes obtained from the iterative normalization method are further corrected based on the orthogonalization property of the unitary matrix, providing the mode shapes satisfying both the normalization and orthogonalization conditions. In Fig. 17 we present the evolution of the mode shapes along these three steps.

Supplementary Note 8. Experimental observation of edge state localization

As explained in Section 3A, in order to observe well-hybridized edge states instead of localized ones, the disorder in the cavity frequencies needs to be low enough. The physical quantity to compare the disorder to are the coupling rates J, J' between the array sites. We say that the disorder is low enough when it's negligible compared to the coupling rates. The device shown in the main text belongs to a second generation design. The first generation design, visible in Fig. 18a featured a different inductor design and the coupling rates were lower: $J' = 127$ MHz, $J = 260$ MHz by fitting the hybridized modes' frequencies with an SSH model. The superconducting optomechanical array was also inductively coupled to input-output waveguides, albeit with a different, microstrip, geometry. In Fig. 18 we show a 12

site topological realization of this generation of devices. Thanks to the use of two circulators on the two input/output ports of the chip this device could be measured either in transmission or in reflection from both sides. Firstly, we see in the transmission spectrum (18b-c) that the edge modes have abnormally low transmission, even though their current density at the edges should be very big, resulting in a great external coupling rate. This is because the edge states are actually localized at one of the edges each. This can be seen in the reflection measurements in Fig. 18d where when we look at the reflection from one side we see only one of the topological peaks, and the other one is only visible at the opposite side of the array. The horizontal axis in subpanels c and d are the same.

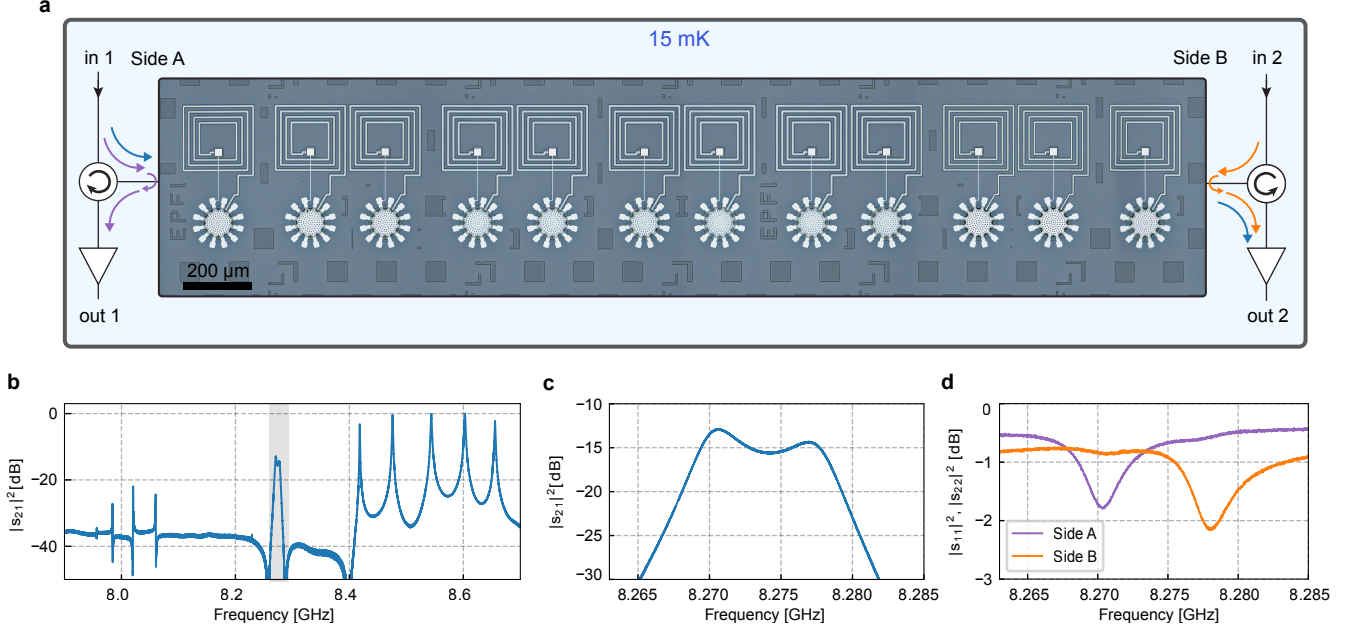


FIG. 18. **Experimental evidence of edge state localization.** **a**, First generation 12-site topological SSH array measured with reflection capabilities from both sides. **b-c**, VNA S_{21} transmission measurement of the device. **d**, VNA S_{11} measurements from both sides of the device. The horizontal axis is the same as **c**.

Supplementary Note 9. Full device characterisations

A. Samples parameters

The hybridised modes frequencies ω_c and line-widths κ (Tab. I and III) were measured at the VNA then fitted with a complex $s_{21}^{\text{exp}}(\omega) = s_{21}^{\text{Lor}}(\omega) + x + iy$ expression that also takes into account any non-ideal Fano effect. $s_{21}^{\text{Lor}}(\omega)$ is a Lorentzian lineshape and $x + iy$ is a complex displacement that even though it doesn't physically interpret the origin of the 'Fanones', it enables us to model it out. For the cavity and mechanical resonance frequencies, the uncertainty in the values is many orders of magnitude smaller than the least significant reported digit.

The mechanical frequencies (Tab. II and IV) were measured in a similar way, doing an OMIT measurement, and fitting the VNA trace with an $s_{11}^{\text{exp}}(\omega)$ reflection Lorentzian experimental profile. The bare mechanical damping rates Γ_m were extracted by taking the intercept of the Γ_{eff} fits versus power. For a fixed mechanical site, more than one independent value of Γ_m was extracted by looking at the different hybridised modes. What we are reporting here is the weighted average of such values. The error in these measurements is of the same order of magnitude of the digit in round brackets.

Hybridized mode	10	9	8	7	6	5	4	3	2	1
$\omega_c/2\pi$ [GHz]	8.463	8.139	7.767	7.435	7.016	6.922	6.590	6.404	6.285	6.216
$\kappa/2\pi$ [MHz]	3.904	4.556	4.176	4.668	4.964	7.09	0.696	0.384	0.239	0.080

TABLE I. 1D hybridized cavity modes parameters

Site number	1	2	3	4	5	6	7	8	9	10
$\Omega_m/2\pi$ [MHz]	2.142	2.165	2.202	2.238	2.267	2.315	2.616	2.405	2.448	2.506
$\Gamma_m/2\pi$ [Hz]	4.3(3)	4.2(3)	12.(1)	11.(1)	15.(4)	12.(2)	15.(2)	8.(0)	16.(6)	10.6(3)

TABLE II. 1D mechanical modes parameters

Hybridized mode	24	23	22	21	20	19	18	17	16	15	14	13
$\omega_c/2\pi$ [GHz]	8.250	7.926	7.851	7.667	7.644	7.512	7.494	7.481	7.401	7.374	7.224	7.189
$\kappa/2\pi$ [MHz]	4.79	4.601	4.485	1.09	6.468	2.165	2.504	1.027	3.31	2.002	0.349	0.362
Hybridized mode	12	11	10	9	8	7	6	5	4	3	2	1
$\omega_c/2\pi$ [GHz]	7.100	7.068	6.911	6.896	6.871	6.837	6.829	6.797	6.772	6.750	6.717	6.671
$\kappa/2\pi$ [MHz]	0.265	0.766	4.36	1.121	0.241	0.174	2.635	1.603	1.261	0.532	1.308	0.456

TABLE III. 2D hybridized cavity modes parameters

Site number	1	2	3	4	5	6	7	8	9	10	11	12
$\Omega_m/2\pi$ [MHz]	82.106	2.127	2.158	2.179	2.208	2.233	2.260	2.291	2.314	2.347	2.380	2.413
$\Gamma_m/2\pi$ [Hz]	43.(7)	9.(0)	6.(9)	4.(1)	15.(6)	12.(6)	14.(1)	6.0(9)	29.(8)	8.(1)	20.(5)	3.2(7)
Site number	13	14	15	16	17	18	19	20	21	22	23	24
$\Omega_m/2\pi$ [MHz]	2.435	2.469	2.501	2.539	2.571	2.611	2.648	2.672	2.708	2.749	2.796	2.836
$\Gamma_m/2\pi$ [Hz]	5.(5)	10.(8)	6.7(7)	6.(4)	16.(3)	9.(8)	39.(0)	20.(5)	18.(6)	10.(3)	8.(9)	18.(1)

TABLE IV. 2D mechanical modes parameters

B. Measurement of optomechanical coupling rate

In order to measure $\eta_i^k g_{0,i}$, the effective optomechanical coupling rate between collective microwave mode k and mechanical oscillator i , we characterize the mechanical sideband induced by a resonant microwave drive. In contrast to the measurement of the optomechanical damping rate, we set the drive power so that the cooperativity can be about 1 to minimize the measurement backaction on the phonon occupation. We measure the power spectrum density (PSD) of the upper sideband signal and integrate the PSD to obtain the total power. From Eq. (17), the sideband power [14] scaled to photon flux is given by

$$n_{\text{sb}} = G^k \frac{\kappa_2^k}{\kappa_{\text{tot}}} \frac{\kappa_{\text{tot}}^k (\eta_i^k g_{0,i})^2 n_c^k}{\Omega_{m,i}^2 + \kappa_{\text{tot}}^k / 4} n_{m,i}, \quad (52)$$

where G^k is the gain of the full measurement chain from the device, κ_2^k is the external coupling rate to the output line, and $n_{m,i}$ is the phonon occupation of mechanical oscillator i . The intracavity photon number with the resonant drive is explicitly described as

$$n_c^k = \frac{4\kappa_1^k}{\kappa_{\text{tot}}^k} R^k n_{d,\text{in}}, \quad (53)$$

where R^k is the transmittance between the device and a microwave source used for the drive, κ_1^k is the external coupling rate to the input line, and $n_{d,\text{in}}$ is the drive power scaled to photon flux at the output of the microwave source. From the scattering parameters based on the input-output formalism [17], the transmitted drive power scaled to photon flux is given by

$$n_{d,\text{out}} = G^k \frac{4\kappa_1^k \kappa_2^k}{\kappa_{\text{tot}}^k} R^k n_{d,\text{in}}, \quad (54)$$

where we assume that the gain G^k and transmittance R^k does not have frequency dependence between the drive and the mechanical sideband. Using Eqs. (52), (53), and (54), we obtain

$$\frac{n_{\text{sb}}}{n_{d,\text{out}}} = \frac{(\eta_i^k g_{0,i})^2}{\Omega_{m,i}^2 + \kappa_{\text{tot}}^k / 4} n_{m,i}. \quad (55)$$

Note that all the parameters that would be challenging to obtain experimentally, except for the effective optomechanical coupling rate $\eta_i^k g_{0,i}$, are canceled out in this expression, enabling us to determine the coupling rate.

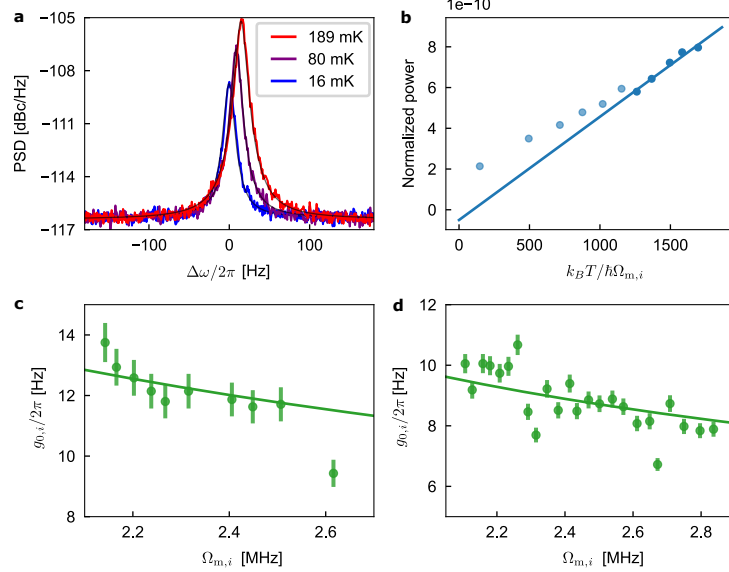


FIG. 19. **Measurement of optomechanical coupling rate.** **a**, Power spectrum density (PSD) of the upper mechanical sideband with the different base temperatures of the dilution refrigerator. The black lines are the Voigt function fits to extract the total power of the sideband. **b**, Normalized total power of the mechanical sideband as a function of the nominal phonon occupation, calculated from the base temperature. The dots are the experimental results and the line is the linear fit to the data in the higher temperature region (dark blue). **c,d**, Single-photon optomechanical coupling rate at site i for the 1D chain and 2D lattice, respectively. The lines are inverse square root fits.

We calibrate the phonon occupation $n_{m,i}$ by increasing the temperature of the environment for the device so that the mechanical oscillator can be thermalized, i.e. $n_{m,i} \approx k_B T / \hbar \Omega_{m,i}$, where T is the base temperature of the dilution refrigerator. Figure 19a shows the PSD of the mechanical sideband of mechanical mode $i = 6$ induced by the resonant drive to collective microwave mode $k = 10$ of the 1D chain. Since the minimum resolution bandwidth of the spectrum analyzer is comparable with the mechanical linewidth, we extract the total power of the mechanical Lorentzian peak by fitting the PSD with a Voigt function with the Gaussian bandwidth corresponding to the resolution bandwidth. Figure 19b shows the sideband power normalized by the transmitted drive power as a function of the nominal phonon occupation calculated by $k_B T / \hbar \Omega_{m,i}$. In the region of the higher temperature, the normalized sideband power follows linearly the nominal phonon occupation, so that we can assume it is thermalized. By fitting the slope in this region, the effective optomechanical coupling rate can be extracted as

$$(\eta_i^k g_{0,i})^2 = \frac{\partial(n_{\text{sb}}/n_{\text{d,out}})}{\partial n_{m,i}} \left(\Omega_{m,i}^2 + \kappa_{\text{tot}}^k / 4 \right), \quad (56)$$

where all the remaining parameters are determined from independent measurements. Using the data shown in Fig. 19b, the optomechanical coupling rate between the collective microwave mode and the mechanical oscillator is found to be $(\eta_i^k g_{0,i})/2\pi = 2.2$ Hz for $k = 10$ and $i = 6$. Using the known participation ratio η_i^k , the optomechanical coupling rate at site i is found to be $g_{0,i}/2\pi = 12$ Hz for $i = 6$.

Since all the participation ratio η_i^k are determined as discussed in Sec. 1B, all the optomechanical coupling rate $g_{0,i}$ are determined as follows. Form the optomechanical damping rate, the unnormalized participation ratio $\tilde{\eta}_i^k$ is experimentally obtained by Eq. (22). Using the relation described in Eq. (23), the relative optomechanical coupling rate at site i can be determined as

$$\bar{g}_{0,i} = \frac{g_{0,i}}{\sum_i g_{0,i}} = \frac{\left(\tilde{\eta}_i^k / \eta_i^k \right)}{\sum_i \left(\tilde{\eta}_i^k / \eta_i^k \right)}. \quad (57)$$

We obtain the relative coupling rate using the mode shapes for $k = 10$ of the 1D chain. From the mechanical sideband measurement, we have already known one of the optomechanical coupling rate, i.e. $g_{0,i'}$ for $i' = 6$ in our case. Thus,

the optomechanical coupling rate at site i is determined as

$$g_{0,i} = \frac{\bar{g}_{0,i}}{\bar{g}_{0,i'}} g_{0,i'}. \quad (58)$$

Figure 19c shows all the optomechanical coupling rate between the bare microwave mode and the mechanical oscillator at site i of the 1D chain. We apply the same measurement and analysis for the 2D lattice. All the optomechanical coupling rates in the 2D lattice are determined as shown in Fig. 19d.

As shown in Figs. 19c and d, the single-photon optomechanical coupling rates are fitted well to the inverse of the square root of the mechanical frequency. This can be interpreted by the fact that the zero-point fluctuation of motion of a mechanical oscillator is proportional to the inverse of the square root of the mechanical frequency, i.e. $x_{\text{ZPF}} = \sqrt{\hbar/(2m_{\text{eff}}\Omega_m)}$, where m_{eff} is the effective mass [1].

C. 2D modeshapes and Hamiltonian reconstruction

Even though in the main text we report only 6 mode shapes for the 2D honeycomb lattice, we were able to measure all 24 of them. These can be seen in the full page Fig. 20. For some of them the agreement is not as good as we observed in the 1D case. This is because, given the much higher number of resonators, the effect of disorder plays a more important role. Where the dots are completely missing it means that the experimental power participation ratio η_i^k of site i to the collective microwave mode k was not high enough to produce a detectable signal, or any significant cooling.

Using the extracted mode shapes of 2D device, we can use the same approach presented in the main text to calculate the closest unitary matrix to the eigenmodes (\mathbf{U}_ψ) and reconstruct the Hamiltonian. Figure 21 shows the reconstructed Hamiltonian matrix in the rotating frame versus the ideal designed Hamiltonian including SNN couplings. Due to the higher disorder in the measured mode shapes of the 2D sample, as discussed in the inner product section, the unitary matrix and consequently Hamiltonian are slightly more disturbed compared to the 1D case, however still show well agreement with the design and theoretical predictions.



FIG. 20. **All 24 measured mode shapes of the 2D device.** The amplitude of the mode shape $|\psi_i^k|$ is encoded in the area of the circles. Only for modes that share the same colorbar the size or color of the circles can be compared. Highlighted in purple are the four edge modes in the bandgap.

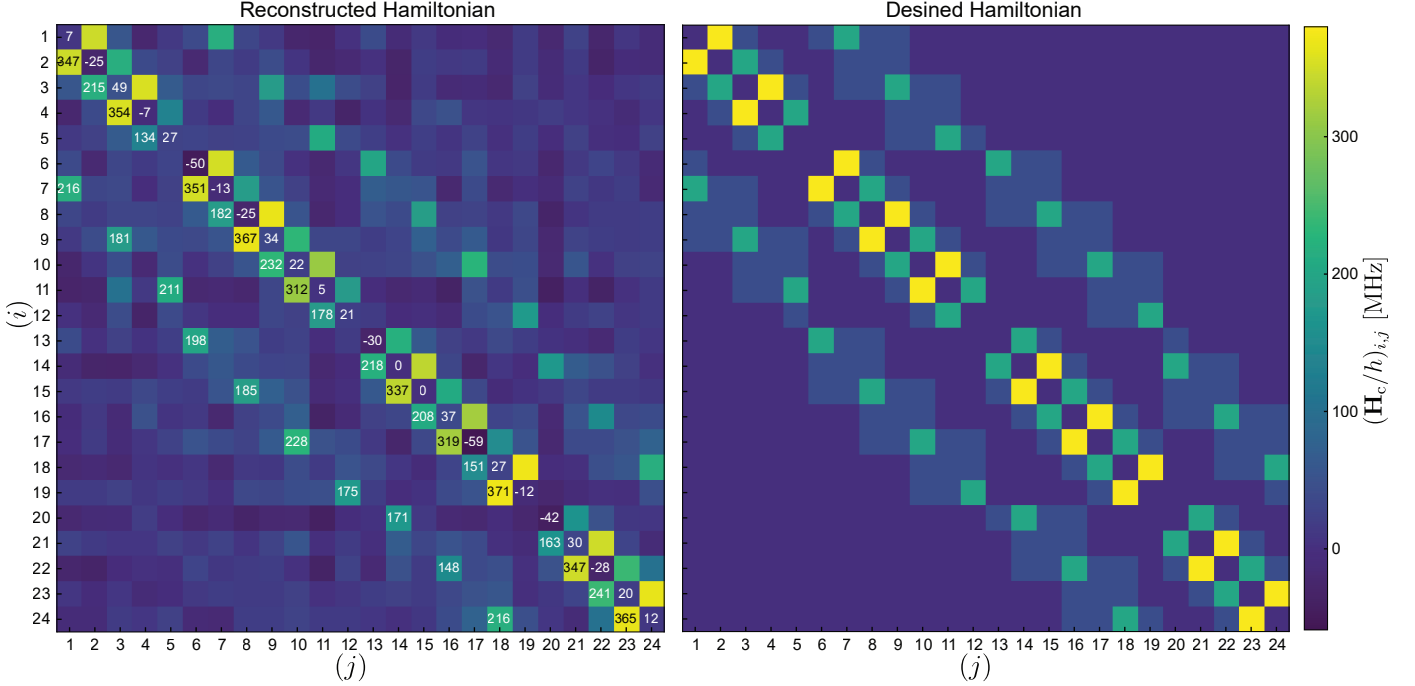


FIG. 21. **Hamiltonian reconstruction of the 2D honeycomb lattice.** The reconstructed Hamiltonian of 24 site 2D honeycomb device (left) and the designed Hamiltonian including second nearest neighbor couplings (right). The diagonal elements represent the individual site's resonance frequency deviation from the average bare cavity frequency.

Supplementary References

* These authors contributed equally.

† tobias.kippenberg@epfl.ch

- [1] M. Aspelmeyer, T. J. Kippenberg, and F. Marquardt, Cavity optomechanics, *Reviews of Modern Physics* **86**, 1391 (2014).
- [2] L. Li, Z. Xu, and S. Chen, Topological phases of generalized su-schrieffer-heeger models, *Physical Review B* **89**, 085111 (2014).
- [3] B. Pérez-González, M. Bello, Á. Gómez-León, and G. Platero, Ssh model with long-range hoppings: topology, driving and disorder, *arXiv preprint arXiv:1802.03973* (2018).
- [4] B. Pérez-González, M. Bello, Á. Gómez-León, and G. Platero, Interplay between long-range hopping and disorder in topological systems, *Physical Review B* **99**, 035146 (2019).
- [5] L. Li, N. Hao, G. Liu, Z. Bai, Z.-D. Li, S. Chen, and W.-M. Liu, Quantum Hall Effects in a Non-Abelian Honeycomb Lattice, *Physical Review A* **92**, 063618 (2015), arXiv: 1506.00125.
- [6] Y. Hasegawa and M. Kohmoto, Quantum Hall effect and the topological number in graphene, *Physical Review B* **74**, 155415 (2006), arXiv: cond-mat/0603345.
- [7] Y. Zhang, Y.-W. Tan, H. L. Stormer, and P. Kim, Experimental observation of the quantum hall effect and berry's phase in graphene, *nature* **438**, 201 (2005).
- [8] Y.-H. Li and R. Cheng, Magnonic su-schrieffer-heeger model in honeycomb ferromagnets, *Physical Review B* **103**, 014407 (2021).
- [9] M. Fujita, K. Wakabayashi, K. Nakada, and K. Kusakabe, Peculiar localized state at zigzag graphite edge, *Journal of the Physical Society of Japan* **65**, 1920 (1996).
- [10] K. Cicak, D. Li, J. A. Strong, M. S. Allman, F. Altomare, A. J. Sirois, J. D. Whittaker, J. D. Teufel, and R. W. Simmonds, Low-loss superconducting resonant circuits using vacuum-gap-based microwave components, *Applied Physics Letters* **96**, 093502 (2010).
- [11] J. D. Teufel, D. Li, M. Allman, K. Cicak, A. Sirois, J. Whittaker, and R. Simmonds, Circuit cavity electromechanics in the strong-coupling regime, *Nature* **471**, 204 (2011).
- [12] J. Suh, A. Weinstein, C. Lei, E. Wollman, S. Steinke, P. Meystre, A. A. Clerk, and K. Schwab, Mechanically detecting and avoiding the quantum fluctuations of a microwave field, *Science* **344**, 1262 (2014).
- [13] J.-M. Pirkkalainen, E. Damskägg, M. Brandt, F. Massel, and M. A. Sillanpää, Squeezing of quantum noise of motion in a micromechanical resonator, *Physical Review Letters* **115**, 243601 (2015).
- [14] L. D. Toth, N. R. Bernier, A. Nunnenkamp, A. Feofanov, and T. Kippenberg, A dissipative quantum reservoir for microwave light using a mechanical oscillator, *Nature Physics* **13**, 787 (2017).
- [15] L. D. Tóth, *Dissipation as a resource in circuit quantum electromechanics*, Tech. Rep. (EPFL, 2018).
- [16] L. D. Tóth, N. R. Bernier, A. Nunnenkamp, A. K. Feofanov, and T. J. Kippenberg, A dissipative quantum reservoir for microwave light using a mechanical oscillator, *Nature Physics* **13**, 787–793 (2017).
- [17] A. A. Clerk, M. H. Devoret, S. M. Girvin, F. Marquardt, and R. J. Schoelkopf, Introduction to quantum noise, measurement, and amplification, *Reviews of Modern Physics* **82**, 1155 (2010).